International Journal of Concrete Structures and Materials

RESEARCH

Open Access

Pore Structure Characterization and Environmental Assessment of Ground Volcanic Pumice-Based Alkali-Activated Concrete

Mohammed Ibrahim[1*], Ashraf A. Bahraq[2], Babatunde Abiodun Salami[3], Luai Mohammed Alhems[1], Syed Rizwanullah Hussaini[4], Muhammad Nasir[5] and Adeshina Adewale Adewumi[6]

Abstract

The impact of pore structure and its connectivity in ground volcanic pumice (GVP) and nano-silica (nSi)-based AAB on the chloride diffusion leading to corrosion of reinforcing steel for a period of up to 2.5 years was investigated in this study. ^{1}H proton NMR relaxometry was employed as an innovative method to examine the pore structure and connectivity in alkali-activated concrete (AAC), in conjunction with the assessment of bulk chloride diffusion. Alkali-activated GVP with marginal quantities of nSi outperformed similar grade conventional OPC concrete when exposed to bulk diffusion in accordance with ASTM C1556. There was nearly 80–90% reduction in chloride diffusivity in 5.0% and 7.5% nSi mixes and 60% increase in compressive strength. The contour maps showed that nSi incorporation greater than or equal to 5.0% significantly lowered porosity, enabled poor pore connectivity and minimized chloride diffusion, resulting in enhanced protection against chloride-induced corrosion of steel rebar in the AAC. It was revealed that the remarkable resistance of nSi-modified GVP-AAC to the aggressive environment was attributed to the better polymerization and physical influence enhanced the binder structure. The environmental assessment results showed that GVP-based alkali-activated mixes reduced CO_2 emissions by 53% to 60% compared to the OPC-based mix, demonstrating their strong potential for lowering the carbon footprint of concrete.

Keywords Ground volcanic pumice, Nanosilica, Alkali-activated concrete, ^{1}H proton NMR relaxometry, Pore structure, Chloride diffusion, Chloride-induced corrosion, LCA study

Journal information: ISSN 1976-0485 / eISSN 2234-1315.

*Correspondence:
Mohammed Ibrahim
ibrahim@kfupm.edu.sa
[1] Applied Research Center for Metrology, Standards and Testing, Research Institute, King Fahd University of Petroleum & Minerals, 31261 Dhahran, Saudi Arabia
[2] Interdisciplinary Research Center for Construction and Building Materials, King Fahd University of Petroleum & Minerals, 31261 Dhahran, Saudi Arabia
[3] Cardiff School of Management, Cardiff Metropolitan University (Landaff Campus), Cardiff CF5 2YB, UK
[4] Centre for Integrative Petroleum Research, College of Petroleum Engineering & Geosciences, King Fahd University of Petroleum & Minerals, 31261 Dhahran, Saudi Arabia
[5] Department of Civil and Construction Engineering, College of Engineering, Imam Abdulrahman Bin Faisal University, 31451 Dammam, Saudi Arabia
[6] Department of Civil Engineering, University of Hafr Al Batin, 31991 Hafr Al-Batin, Saudi Arabia

1 Introduction

The cement industry, a vital component of global infrastructure, is paradoxically one of the most significant contributors to climate change, responsible for approximately 2.8 billion tons annually (Khaiyum et al., 2023). Despite the daunting environmental impact, a lot of advancements have been made to mitigate these emissions. From 1930 to 2021, the cumulative global CO_2 uptake by cement materials was estimated to be 22.9 gigatons (Gt), offsetting 55.1% of the emissions from cement production over the same period. Looking ahead, the future of cement production is poised for transformation (Huang et al., 2023). By 2060, the integration of low-carbon technologies such as re-engineering mixture designs for microstructure enhancement, alternative raw materials and fuels, enhanced energy efficiency, and carbon capture and storage (CCS) is predicted to significantly curb the industry's carbon footprint (Xu et al., 2023a). Among these innovations, re-engineering the mixture design for microstructure enhancement stands out as a critical approach. This method not only improves the performance and durability of cement, but also substantially reduces its carbon emissions, promising a more sustainable path forward for the industry (Gao et al., 2023). Furthermore, the durability of concrete is a prevalent challenge encountered by many countries, and the expenses associated with repairing and retrofitting deteriorating structures can be substantial. In the absence of effective measures to prevent and address this problem, deterioration can have a negative impact on the quality of the built environment (Tran et al., 2021). As per the ASCE's 2021 Review for America's Infrastructure (ASCE, 2021), the United States presently allocates approximately $1.6 trillion towards infrastructure maintenance and enhancements, which encompasses addressing concrete deterioration due to durability. According to the Global Competitiveness Report 2018 by the World Economic Forum (Schwab, 2018), it is estimated that the worldwide shortfall in infrastructure investment for repairing decaying concrete amounts to approximately $15 trillion.

In response to regulatory measures and global efforts to reduce environmental impact, building materials researchers have focused on developing sustainable alternatives, such as alkali-activated binders (AABs). Extensive research has been conducted in recent years on the synthesis, polymerization mechanism, and evaluation of the fresh, hardened, durability, and microstructural properties of AABs produced from a variety of industrial solid waste and by-products in the presence of various alkaline activators (Fan et al., 2025; Ibrahim & Maslehuddin, 2021; Kumar et al., 2023; Salami et al., 2016, 2017a, 2017b, 2018; Xue et al., 2023). In contrast to the layered structure of C–S–H gel that results from the hydration of OPC in the presence of water that precipitates in the pores, these literature reviews concluded that the interaction between aluminosilicious precursor materials and highly alkaline materials produces a polymeric structure with abilities to support loads and survive varying environmental conditions. The AABs are formed in three stages of dissolution, gelation, and poly-condensation. The degree of polymerization determines the mechanical strength and durability to resist penetration of harmful agents that are believed to be responsible for the degradation of binder structure.

OPC-based cementitious binders' matrix constitutes heterogeneous multiphase porous solids. Depending on precipitation and the degree of hydration, the pore structure and pore connectivity are developed in the binder structure, which plays a crucial role in imparting strength and serviceability. Poor pore structure and better pore connectivity may lead to the incessant ingress of chloride ions, thereby decreasing the pH of the surrounding concrete and therefore causing the corrosion of reinforcing steel. Consequently, it jeopardizes the service life of the reinforced concrete structures. Hence, the evaluation of physical parameters such as pore structure is essential in order to fully understand the kinetics involved in the cementitious binder (Mohammed et al., 2023; Nazari Sam et al., 2023; Salami et al., 2014; Toma et al., 2023).

Hitherto, a few techniques, including nitrogen adsorption, backscattered electron image analysis, and mercury intrusion porosimetry (MIP), have been employed to examine the pore structure of cementitious materials. Among them, MIP has been extensively utilized for this purpose, which involves high pressure to drive mercury into the pores that may damage the integrity of the pore structure (Chalid, 2021). In addition, the accuracy of the results depends on the interaction of mercury with the pore fluid nature, mobility, and concentration (Golež et al., 2023). Since this technique does not measure the whole pore size but only the size of the pore throat, the estimation of large pores may be miscalculated (Ryukhtin et al., 2023). Furthermore, the procedure's use of highly toxic liquid mercury poses significant risks to public health and safety, as well as environmental hazards (Xu et al., 2023b).

In the recent past, the application of nuclear magnetic resonance (NMR) to examine the efficacy of building materials has been limited. It has been utilized to investigate the early-age cement hydration process with time, along with the intensity and extent of water trapped in the pores (Ojo & Mohr, 2009). In addition, it has also found use in explaining how the cement admixtures influence the reaction mechanism and formation of cement hydration products with respect to the curing

period. Gussoni et al. (2004) employed the NMR technique to assess the dynamic process of hydration and the progression of pore structure. They identified prominent substances, which are hydration products and liquids that are entrapped as free water in the pores. In another study (Bligh et al., 2016), the gel pore formation and water in the layered structure of C–S–H were examined during the early hydration of cement. Moreover, the influence of admixtures to retard the hydration process of cement was also investigated at various ages, which demonstrated the addition of retardants towards prolonging the setting times of cement. Elsewhere (Oligschläger et al., 2014), spin density and T_2 relaxation time were studied to identify three stages of cement curing. For instance, when the water is mixed with cementitious powder, it starts hydrating. In the initial stage, due to the presence of a large amount of water, the relaxation time measured was long, about 15 min. In the second stage, as the hydration products are being formed, spin density along with measurable relaxation time T_2 could be recorded, which may take between 1 and 2 h of mixing time. Furthermore, the hydration products are slowly formed and start filling the larger pores. This phenomenon decreases free water in the mixture, and this is a third stage in the hydration process in which relaxation time and the spin density significantly decreased. As the amount of water in the mixture decreases with duration, the time taken to probe the water decreases, leading to a reduction in the spin density as well. McDonald et al. (2010) examined the NMR signals as a function of the weight of the sample in a controlled drying process to find the extent of loss of water and hydrogen bonds during the hydration reaction. In order to do that, the sample was dried in three stages: firstly, to remove moisture between the layers of C–S–H; secondly, to remove moisture from within the C–S–H gel; and finally, water was entrapped in the pores. As a result, the authors identified the various stages of cement hydration.

Though it is rather complex to establish pore structure evolution due to the hydration of cement, an overview presented in the preceding section clearly points towards the fact that non-destructive techniques such as NMR relaxometry can be employed to identify the stages of cement hydration, thereby detecting the pores network and formation of the hydration products. In the past, attempts have been made to establish a correlation between the pore structure of cementitious materials and their resistivity (Koleva et al., 2008; Lübeck et al., 2012; Ma et al., 2015; McCarter et al., 1999; Zhang & Li, 2009). However, none of the studies focused on the synergistic effect of pore structure and connectivity on chloride ion ingress in AABs. Hence, in this current study, the NMR relaxometry is not only utilized to assess the pore structure and pore connectivity of ground volcanic pumice (GVP)-based AAB, but also its influence on chloride ion ingress was methodically studied. Consequently, the relationship between the pore connectivity and penetration of chloride ions to some extent was established, and its impact on the corrosion of reinforcing steel due to the transport of chloride ions in the alkali-activated concrete (AAC) was monitored over a period of about 2 years of exposure to a corrosive environment. In addition, the life cycle assessment (LCA) was conducted to quantify the environmental impact of the developed mixes. Findings from this study will offer valuable insights towards understanding the effects of the pore structure of GVP-based AAC, encourage the use of ^{1}H proton NMR relaxometry, promote waste valorization and carbon neutrality, and enhance the durability performance and life span of concrete structures exposed to chloride-laden regimes.

2 Experimental Program

2.1 Materials

In this study, the ground volcanic pumice (GVP) plentifully accessible in the western part of Saudi Arabia was utilized as the primary precursor. Figure 1 illustrates the chemical composition of GVP. The characteristics of the utilized colloidal nano-silica (nSi), of which particulates comprised 50% by weight, are presented in Table 1. The alkaline activators utilized were a combination of $NaOH_{aq}$ (molarity = 14) and industrial-grade Na_2SiO_{3aq} (silica modulus = 3.33).

The GVP used in this study was sourced from the Harrat Khaybar volcanic field in the western part of Saudi Arabia. The chemical composition is detailed in Table 1 from X-ray fluorescence (XRF) analysis confirming the major component at 99.52% by weight. The purity levels meet the ASTM C618 standards for pozzolanic materials. The industrial standard nano-silica (nSi) was obtained and has a purity of 99.5% as per the supplier specifications. The specific surface area was 80.5 m^2/g, and the average particle size was 35.5 nm. The GVP was initially oven-dried at 105 °C for 24 h to remove any moisture content. It was then ground to a fineness of 45 µm using a ball mill to ensure uniformity in particle size distribution. No additional chemical treatments were applied. The nSi was used as received from the supplier without further modification. Prior to incorporation into the mixture, the nSi was dispersed in water using a high-shear mixer to prevent agglomeration. The GVP had an average specific gravity of 1.35 and a water absorption rate of 0.45%. The particle size distribution of GVP is shown in Fig. 2. The figure shows a particle size distribution peaking around 10 µm, with the highest volume percentage at 6%. Most particles are smaller, with a sharp decrease for sizes above 10 µm,

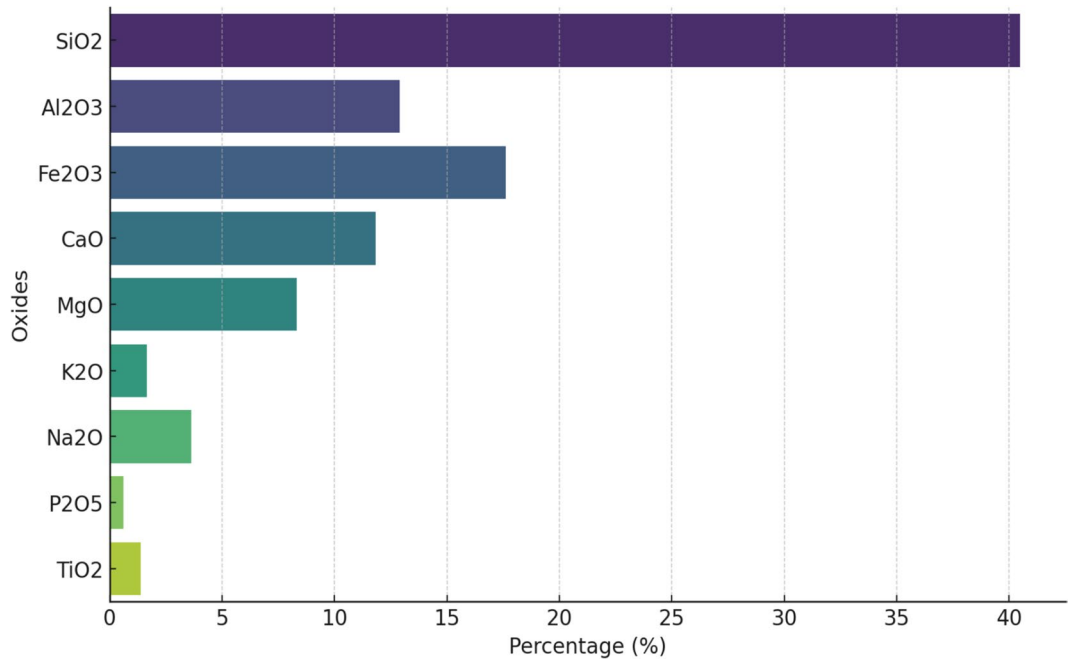

Fig. 1 Oxide composition of GVP

Table 1 Properties of nSi

Parameter	Value
SiO_2	99.52%
Al_2O_3	1.22%
TiO_2	0.029%
Fe_2O_3	0.012%
pH-value	9.55
Mean particle size	35.5 nm
Surface area	80.5 m^2/g
Solid matter content	50%
Density	1.25–1.45 g/cm^3

suggesting a heterogeneous sample with a predominantly small particles and few relatively larger ones. Its use in a binder suggests a microstructure with a high concentration of smaller particles, contributing to a dense and potentially more reactive material. For nSi, the specific gravity was 2.2, and due to its nano-scale size, water absorption was not applicable.

Fine aggregate (FA) has a specific gravity of 2.55 gr/cc and a water absorption of 0.50%. Crushed limestone retrieved from a local quarry was employed as the coarse aggregate (CA) in this research. CA had a specific gravity of 2.61 gr/cc and a water absorption of 1.50%.

2.2 Casting and Curing

2.2.1 Mix Proportions

Table 2 shows the alkali-activated concrete (AAC) mix proportions with varied amounts of nSi (0% to 7.5% by weight of binder). The selection of nSi dosage and its gradient was based on the outcomes of previously published results (Ibrahim et al., 2018). The chosen nSi percentages were informed by prior studies demonstrating their impact on the mechanical and durability properties of alkali-activated binders. Alkali-activated paste (AAP) in 25-mm cube molds was also prepared for micro-analytical analyses. The silica modulus of the total activator's ($Na_2SiO_3 + NaOH$) was 1.351. The alkaline activators accounted for a little more than 50% of the precursor material. With a constant Na_2SiO_3/NaOH ratio of 2.5 by weight, all the AAC mixtures were prepared (M0 to M4). An OPC-based concrete (M5) was prepared using 370 kg/m^3 of OPC and a water-to-cement ratio of 0.45, following industry-standard mix proportions. All samples, including OPC and AAC, were cured under identical conditions.

2.2.2 Sample Preparation and Curing

In preparing the mixture's initial liquid component, the required amount of $Na_2SiO_{3(aq)}$ and $NaOH_{(aq)}$ solutions were added together. Free water and colloidal nSi were eventually added to the solution. The mixture was sonicated for 10 to 12 min using a high-sensitivity ultrasonic processor to achieve a uniform dispersion of the nSi in

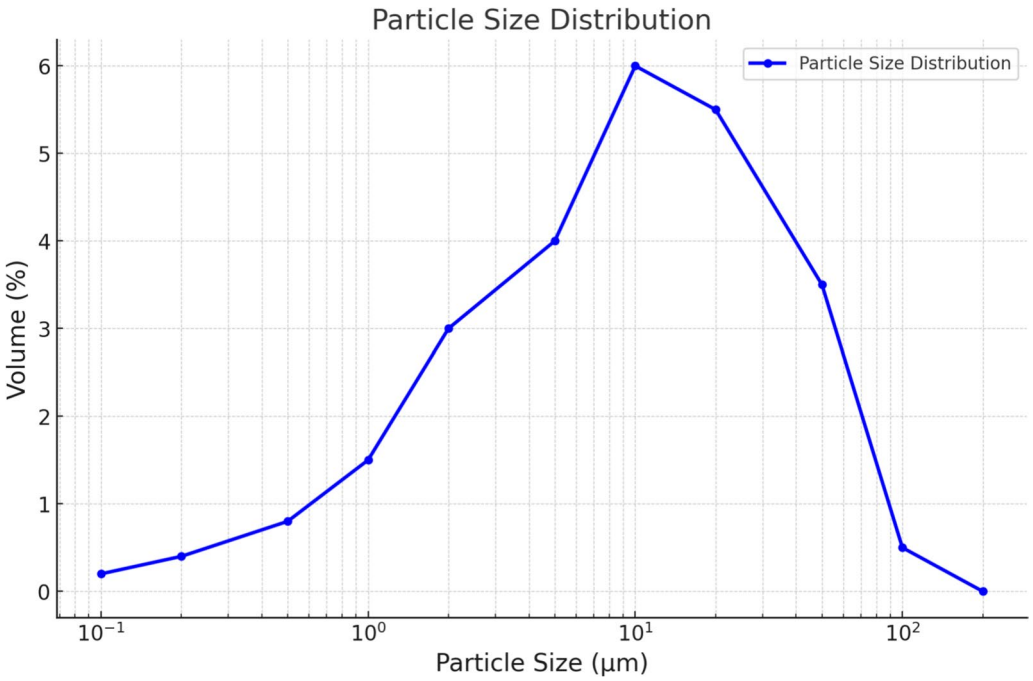

Fig. 2 Particle size distribution of ground volcanic pumice (GVP)

Table 2 AAC mix constituents (kg/m^3)

Mix ID	nSi content	GVP	nSi	Na_2SiO_3	NaOH	FA	CA
M0	0.0%nSi	400.0	0.0	150.0	60.0	650.0	1206.0
M1	1.0%nSi	396.0	8.0			646.0	1200.0
M2	2.5%nSi	390.0	20.0			640.0	1188.0
M3	5.0%nSi	380.0	40.0			630.0	1170.0
M4	7.5%nSi	370.0	60.0			620.0	1152.0

the blend. Next, CA and FA were weighed and put in a Hobart ground-mounted mixer along with the GVP. Initially, these ingredients were mixed in dry state for at least 3 min; afterwards, the liquid component was steadily added to the mixture. To ensure that uniformity was achieved, each ingredient added to the mixing bowl was thoroughly blended. After pouring the mixtures into the molds, they were vibrated to remove air and finished with a trowel. The molds were covered with plastic sheets and stored at a consistent temperature of 23 ± 2 °C and relative humidity of 50 ± 5% for 24 h. The specimens were demolded 24 h after casting. AAC and AAP samples were then sealed in plastic bags to prevent moisture loss and cured for specific duration at the same laboratory conditions. OPC concrete samples were cured under damp burlap for 7 days followed by immersion in water at 23 ± 2 °C until testing. These protocols conform to ASTM C511 standards. These approaches ensure consistent curing conditions, critical for the development of the binder's properties (AlTawaiha et al., 2023).

2.3 Evaluation Methods

2.3.1 Resistance of Concrete to Chloride Penetration

Various standard procedures that measure the resistance of concrete to chloride ion penetration were used in this study. The detailed procedures are presented in the following paragraphs. For each mix, Ø75-mm and 150-mm-high cylindrical concrete specimens were prepared for chloride diffusion test. Following a curing period of 28 days at 23 ± 2 °C and 95% relative humidity, as per ASTM C1556 (ASTM International, 2022), the specimens were left to dry at 50 ± 2 °C for 7 days. The NaCl solution used for diffusion testing was prepared by dissolving 165 g of NaCl in 1 L of distilled water, achieving a concentration of 2.826 M NaCl. The curved and bottom-molded surfaces of the specimens were coated with a

quick-setting two-component epoxy (brand name, type, and specifications). Two coats of epoxy were applied, each allowed to cure for 24 h at room temperature (23 ± 2 °C), ensuring unidirectional chloride ingress. Figure 3 shows the coated specimens and a plastic container used to expose them to the NaCl solution for a predetermined period. The specimens were maintained at a constant temperature of 23 ± 2 °C during the diffusion testing to ensure consistent and controlled environmental conditions. The efficacy of the epoxy coating was validated through visual inspections, which confirmed the absence of visible cracks or defects, and thickness measurements indicating an average coating thickness of 1.5 mm. Preliminary diffusion tests confirmed the impermeability of the coating.

A profile grinder was used to obtain powder samples by grinding parallel to the exposed surface at depths of 0, 2, 4, 6, 8, 10, 12 and 15 mm. Beyond this depth, concrete slices were cut at 20, 50 and 75 mm and ground to obtain a fine powder. Deeper slices were selected to simulate the various concrete covers for the reinforcement in different structural elements. At each depth, 5.0 g of powder was used to evaluate the acid-soluble chloride content. The powder was taken in a 100-ml beaker, to which 10 ml of hot distilled water was added; subsequently, 10 ml of concentrated nitric acid in a diluted form was added. Following the extraction of bonded chlorides by boiling the contents, the solution underwent filtration through a flask, and the filtrate volume was subsequently adjusted to 100 ml. This was utilized for determining the concentration of chloride in the mixtures, which is expressed as a percentage by weight of concrete. The chloride profile and the coefficient of chloride diffusion, as determined by Fick's second law of diffusion (Tennakoon et al., 2017), were evaluated using Eq. (1):

$$C_{x,t} = C_s\left(1 - erf\left(\frac{x}{2\sqrt{Dt}}\right)\right), \tag{1}$$

where $C_{x,t}$ and C_s are the chloride concentrations at depth x corresponding to time t and at the surface, respectively; and D is the coefficient of chloride diffusion.

The rapid chloride permeability test (RCPT) was conducted using a modified test by Noushini and Castel (2018). The modifications included reducing the test duration from 24 to 12 h to accommodate the rapid setting characteristics of the samples, and the non-steady-state migration coefficient, $D_{\text{nssm,}}$ was calculated using Eq. (2) as specified in NT Build 492 (NTB, 1999):

$$D_{\text{nssm}} = \frac{0.0239(273+T)L}{(U-t)t}\left(x_d - 0.0238\sqrt{\left\{\frac{(273+T)Lx_d}{U-2}\right\}}\right), \tag{2}$$

where D_{nssm} is the non-steady-state migration coefficient (measured in 10^{-12} m^2/s); U and T represent the absolute value of the applied voltage and the average value of initial and final temperatures in anolyte solution (°C), respectively; L and x_d are the thickness of the specimen (mm) and the average value of the penetration depth (mm), respectively; and t represent the duration of the test (hour).

2.3.2 Nuclear Magnetic Resonance (NMR) Relaxometry

The emphasis of the current study was on correlating pore connectivity with chloride ion penetration in different concrete mixes. For this purpose, ^{1}H proton nuclear

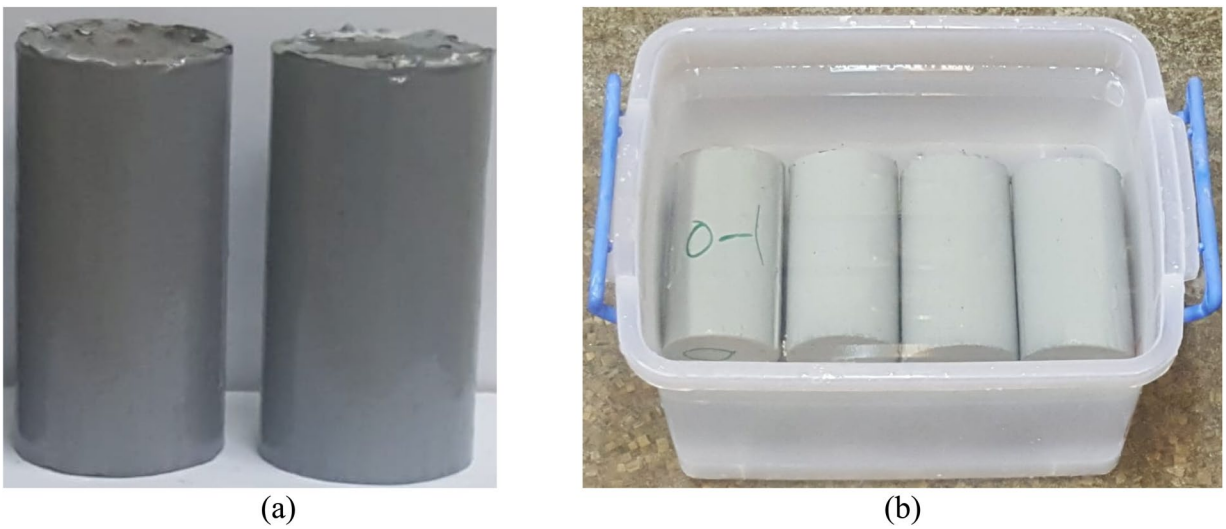

Fig. 3 **a** Coated cylindrical specimens. **b** Exposed specimens in a plastic container

magnetic resonance (NMR) technique was employed to determine the pore structure and pore size distribution of concrete. The NMR analysis on these samples was performed using a GeoSpec2-75 (Oxford Instruments, UK) bench-top Low Field Proton (^{1}H) NMR operating at a resonance frequency of 2.2 MHz. The NMR analyzer was calibrated before each set of measurements using standard reference materials. Calibration checks were performed using a known standard sample of distilled water to ensure the accuracy of the T2 relaxation times. Regular calibration was conducted every 24 h during the testing period to account for any drift in the instrument (Lambert et al., 2024). The NMR analyzer can be used to study samples up to a diameter of 50 mm and a length of 87.5 mm. The Q-Sense signal augmentation technology allows for the identification of very small pores, around 1 nm in size. It consists of a 1-D Pulse Field Gradient amplifier for gradient measurements. In this study, the cylindrical concrete samples having Ø35 mm and 35 mm high were saturated in a 3% KCl and 1% $CuSO_4$ brine in a manual saturator. Precision calipers were used to measure each sample, ensuring dimensions were within a tolerance of ± 0.1 mm. Any deviations from these dimensions were recorded and the affected samples were excluded from the analysis. The initial step involved vacuuming the saturation cell with samples enclosed within, followed by the gradual injection of brine until a stable pressure of 1500 psi was attained. This pressure was sustained for a duration of 2 days, during which monitoring ensured that there was no detectable pressure decline, affirming the thorough saturation of the samples. Repeated NMR measurements were conducted on each sample to verify the reproducibility of the T2 relaxation times, with a standard deviation of less than 2% observed across multiple measurements.

The experiments were consistently performed at a constant field strength, resonating with a frequency of 2.2 MHz, and maintained at ambient temperature. Utilizing the standard Carr–Purcell–Meiboom–Gill (CPMG) pulse sequence, decay curves for T_2-relaxation were generated, with a fixed echo time (TE) value (τ = 0.053 ms) sustained amid consecutive 180° pulses. Sixteen repeat scans were averaged to produce a sole exponential degeneration curve, with the repetition time (TR) spontaneously attuned to 7.5 times the expected T_2 value of 2000 ms between scans. The signal-to-noise ratio (SNR) was consistently kept at 150 throughout the experiments, and triplicate runs were conducted to verify measurement reproducibility.

The software, GIT Systems (GeoSpec2), provides various methods for assessing relaxation, including T_1-relaxation signals via the inversion recovery technique and T_2-relaxation signs using the CPMG pulse sequence (Fairhurst et al., 2015). A "spin echo" (SE) sequence, depicted in Fig. 4, involves repetitive 90° and 180° RF pulses, with critical parameters such as echo time (TE) and repetition time (TR). TE represents the duration between the radio frequency (RF) excitation pulse and the peak of the induced signal from the coil, while TR denotes interval amid successive excitation pulses. The CPMG method employs a pulse sequence with a 90° RF pulse followed by a series of 180° pulses, as illustrated in Fig. 4, with time interval amid the initial 90° and subsequent 180° pulses labeled as τ. Echoes occur at τ intervals subsequent each 180° pulse till signal decay. Post-experiment, mean peak value of each echo is plotted to derive a single exponential decay curve for T_2-relaxation determination. The resulting NMR experiment outputs, depicted in Fig. 5 as (a) T_1- and (b) T_2-relaxation curves, facilitate the determination of T_1 and T_2 relaxation times using Bloch equations, as outlined in Fig. 6. T_1 indicates time taken for magnetization (M_z) to reach 63% of its final value, whereas T_2 indicates the duration for magnetization (M_{xy}) to decrease from its peak value to 37%, as demonstrated in Fig. 5.

In fluid-saturated porous media, the overall T_2-relaxation time of proton spins is determined by three distinct relaxation mechanisms: bulk relaxation, surface relaxation, and diffusion relaxation, all of which operate simultaneously, as outlined in Eq. (3) (Coates et al., 1999):

$$\frac{1}{T_2} = \frac{1}{T_{2\text{bulk}}} + \frac{1}{T_{2\text{surface}}} + \frac{1}{T_{2\text{diffusion}}}, \tag{3}$$

where

$$\frac{1}{T_{2\text{bulk}}} = \frac{1}{T_2^{\circ}} + r_2[C], \tag{4}$$

and

$$\frac{1}{T_{2\text{surface}}} = \rho_2 \left[\frac{S}{V}\right]_{\text{pore}}, \tag{5}$$

$$\frac{1}{T_{2\text{diffusion}}} = \frac{D(\gamma GTE)^2}{12}. \tag{6}$$

Therefore,

$$\frac{1}{T_2} = \frac{1}{T_2^{\circ}} + r_2[C] + \rho_2 \left[\frac{S}{V}\right]_{pore} + \frac{D(\gamma GTE)^2}{12}, \tag{7}$$

where T_2 is T_2-relaxation time minus contrast agent; [C] is the concentration of the paramagnetic component; r_2 is the transversal relaxivity constant; ρ_2 is the surface relaxivity of grains; S/V is the ratio of pore surface to fluid volume; D is the molecular diffusion coefficient of pore

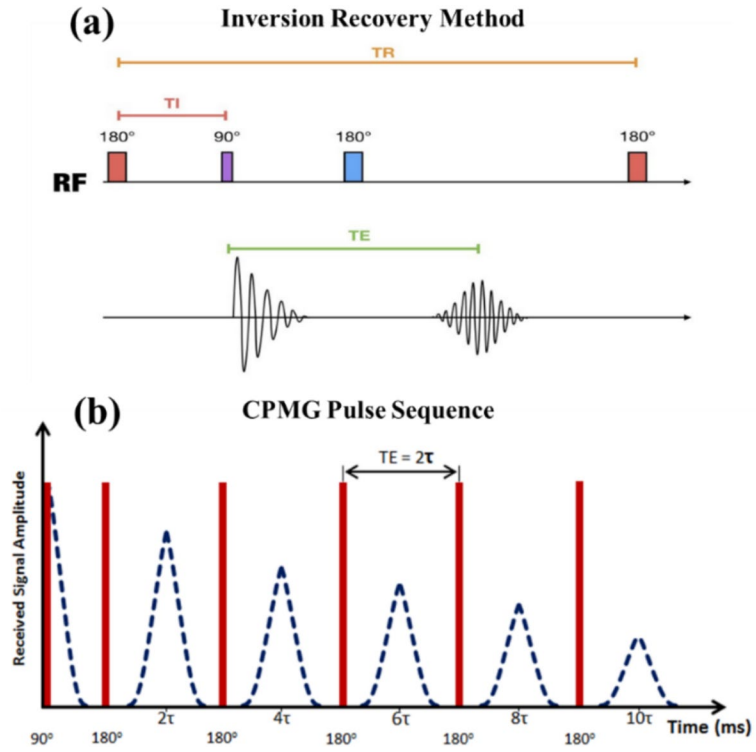

Fig. 4 **a** IR and **b** CPMG pulse sequences (Fairhurst et al., 2015)

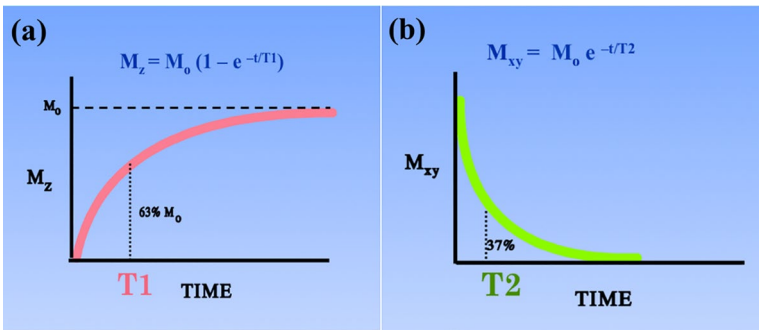

Fig. 5 NMR relaxation curves: a T_1 and b T_2 (Fairhurst et al., 2015)

fluids; γ is the gyromagnetic ratio of a proton nucleus; G is the internal magnetic field gradient (G/cm); and TE is the echo time in the CPMG sequence.

Through the application of Eqs. (4) through (6), Eq. (7) is simplified to characterize the overall T_2-relaxation time of SPIONs solution within porous media. In scenarios of rapid diffusion, the contribution of diffusion relaxation ($T_{2diffusion}$) is negligible in comparison to surface relaxation ($T_{2surface}$), as explained elsewhere (Kenyon, 1997). Additionally, the predominance of surface relaxation is pointed out when employing a shorter TE.

To analyze the diverse fluid components, the NMR T_2-relaxation signal necessitates conversion from a time scale to a continuous 2D T_2-distribution using techniques like inverse-Laplace transform or similar regularization methods. The NMR T_2-signal acquired from the "NMR-GeoSpec2 core analyzer" undergoes automated processing into its constituent components employing GIT software integrated with the spectrometer. These NMR relaxation measurements provide unique insights into the porosity of binding gels (Coates et al., 1999). In scenarios involving multi-component fluids, a standard T_2-relaxation curve not

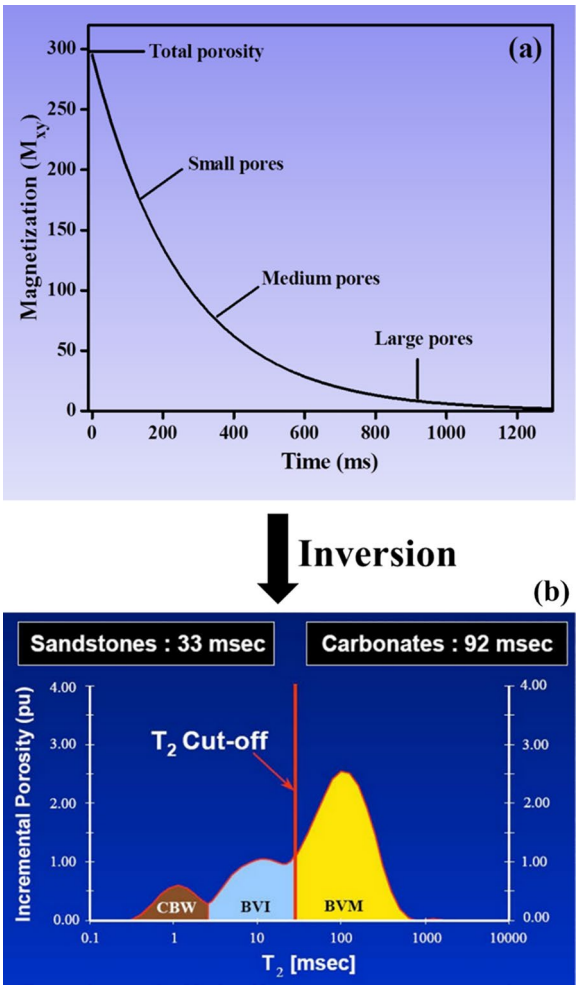

Fig. 6 **a** Standard T_2-relaxation curve and **b** the T_2-distribution obtained through the Laplace inversion technique

only indicates total porosity, but also spots the presence of large, medium, and small pores, as illustrated in Fig. 6a. The conversion of the NMR T_2-relaxation signal to T_2-distribution is achievable through Laplace inversion techniques, as illustrated in Fig. 5b. Typically, the T_2-distribution of any fluid within sandstone or carbonate rocks exhibits a bimodal nature. Total porosity (ϕ_T) is computed as the sum of clay-bound water (CBV), bulk volume irreducible (BVI), and bulk volume movable (BVM), as articulated in Eq. (8) (Fairhurst et al., 2015). Furthermore, effective porosity (ϕ_e) is determined by the combined values of BVI and BVM, as outlined in Eq. (9):

$$\Phi_T = \text{CBV} + \text{BVI} + \text{BVM}, \tag{8}$$

$$\Phi_e = \text{BVI} + \text{BVM}. \tag{9}$$

The model illustrated in Fig. 7 shows fluid-saturated sandstone and defines three key parameters pertaining to intergranular porosity: CBV, BVI, and BVM. CBV denotes water firmly bound to mineral surfaces, impervious to displacement by hydrocarbons, characterized by short T_1 and T_2 relaxation times. BVI represents capillary-bound water, coexisting with immobile fluids, with relaxation times falling between CBV and BVM. BVM suggests the free-fluid index (FFI) and indicates the fractional volume occupied by mobile fluids, comprising water, gas, oil, or their mixtures, exhibiting longer T_1 and T_2 relaxation times compared to BVI and CBV. Analysis of fluid constituents within uniformly shaped pores reveals a direct correlation between T_2 relaxation time and pore size. Larger pores and free-fluid configurations exhibit lower surface-to-volume (S/V) ratios, resulting in extended T_2 relaxation times, whereas smaller pores and bound-fluid arrangements demonstrate higher S/V ratios, leading to shorter T_2 relaxation times, as depicted in Fig. 8. Examination of fluid constituents within non-uniformly shaped pores yields a T_2 relaxation curve involving multiple T_2 values, evident from the T_2-distribution. Consequently, T_2 values are influenced by factors such as pore size and the composition of fluids within pores, including oil, gas, water, or their combinations. In this study, the NMR GeoSpec2 analyzer was employed to determine T_2 relaxation times. Utilizing T_2 relaxation times after 28 and 90 days of curing facilitated the determination of pore structure and connectivity of AAC.

2.3.3 Electrochemical Measurements

Free corrosion potentials (E_{corr}) and corrosion current density (I_{corr}) on steel embedded in the various concrete mixes were measured at regular intervals in accordance with ASTM C876 (ASTM, 2022). These measurements were carried out over a period of 2½-years on the samples immersed in 5% NaCl solution. The concrete specimens used were in a cylindrical shape of size Ø75 mm and height 150 mm having a Ø12 mm rebar centrally placed. A linear polarization scan in the range of ± 10 mV was performed in order to determine polarization resistance (R_p). A scan rate of 7.5 mV/m was adopted. I_{corr} was calculated using the Stern and Geary formula (Stern & Geary, 1957).

2.3.4 Scanning Electron Microscopy (SEM)

SEM analysis was operated using JEOL SEM + EDS model 5800 LV on the interior portions of AAP. An accelerating voltage of 20 kV and scanning electron image mode were set to capture the micrographs at a resolution of 1000–1400 × and at a constant scale of 10 µm.

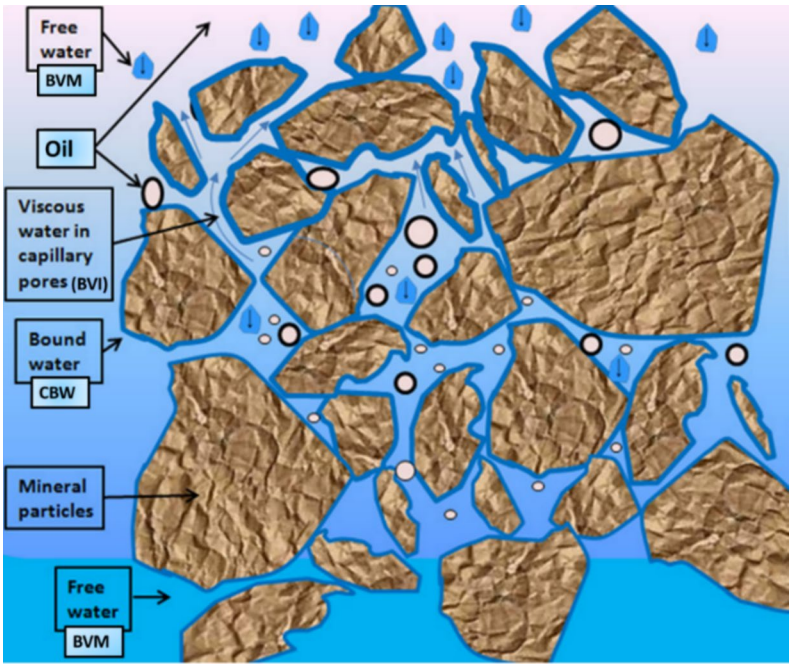

Fig. 7 Fluid-saturated sandstone model representing CBV, BVI, and BVM

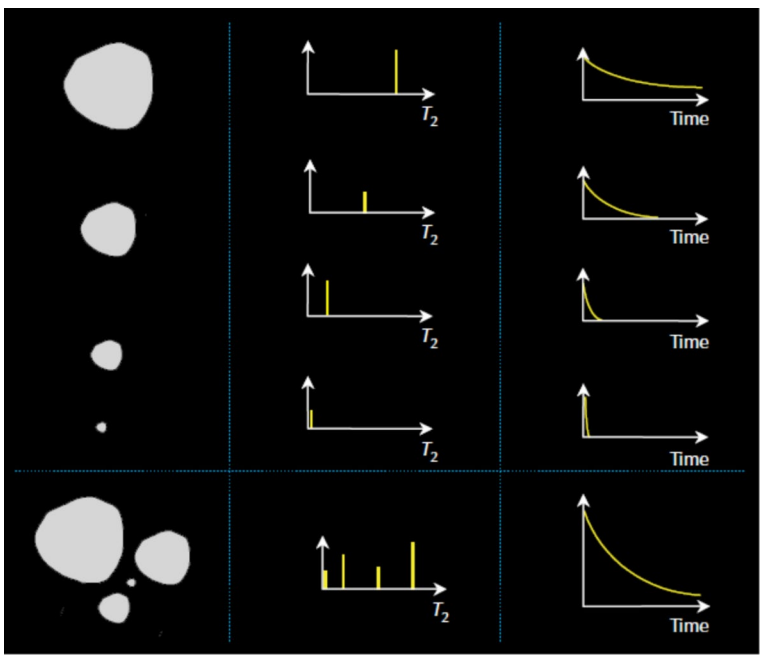

Fig. 8 Assessment of porosity using T_2-relaxation measurements

2.3.5 Environmental Assessment

The life cycle assessment (LCA) of the GVP-based alkali-activated mixes was conducted following the ISO standards (ISO, 2006), with a focus on global warming potential (GWP) as the key environmental impact indicator. A functional unit of one cubic meter of mix was used to compare the GWP of the GVP-based mixes with the conventional OPC-based mix. The CO_2 emissions

of the ingredients were sourced from the Ecoinvent 3.2 database and pertinent literature (Habert & Ouellet-Plamondon, 2016; Maddalena et al., 2018; Nazari, 2017; Nematollahi et al., 2017; Perez-Cortes & Escalante-Garcia, 2020; Robayo-Salazar et al., 2018; Salami et al., 2023). These include OPC (0.898 kg·$CO_{2\text{-eq}}$ /kg), GVP (0.0093), nSi (0.390), FA (0.0023), CA (0.0068), NaOH (0.991), and Na_2SiO_3 (0.425).

3 Results and Discussion

3.1 Resistance of Concrete to Chloride Penetration

After 35 and 90 days of exposure to 2.826 M NaCl solution according to ASTM C1556 (ASTM International, 2022), the total chloride concentration expressed by weight of concrete at various depths from the exposed surface was determined, as displayed in Figs. 9 and 10, respectively. In general, there was a sharp decline in the chloride concentration with increasing depth from the surface of exposure up to a depth of 25 mm. The profile beyond 25 mm depth turns out to be asymptotic to the *x*-axis. This trend was observed in all the mixes at both exposure periods. However, there was a significant difference in the total chloride concentration in the various mixes. At about 0.5 mm from the surface after 35 days of exposure, as displayed in Fig. 11, the chloride concentration in the AAC mixes was approximately 0.65, 0.55, 0.45, 0.35, and 0.32 percent by weight of concrete for mixes containing 0, 1, 2.5, 5, and 7.5 percent nSi, respectively. At a depth of 25 mm, these concentrations decreased to 0.14, 0.05, 0.04, 0.03, and 0.02 percent. Conversely, in OPC concrete, the chloride concentration was about 0.56% at 0.5 mm depth and 0.09% at 25 mm depth. These results indicate considerable resistance to chloride penetration in all concrete mixes. The lowest chloride concentration was observed in the mix with the highest nSi content (7.5%), followed by the mix with 5.0% nSi. There was an 80% to over 90% decrease in chloride concentration as the depth increased from 0.5 mm to 25 mm. The profile trend remained consistent even as the exposure period extended from 35 to 90 days, although the chloride concentration at various depths increased. For example, near the surface, the chloride concentration ranged from 0.9% to 1% in the control GVP-based AAC, 1% nSi-modified, and OPC concrete. It was lowest in the mixes with 5.0% and 7.5% nSi (0.5% to 0.6%, respectively). Significantly lower chloride penetration in these mixes was due to reduced pore connectivity and smaller average pore sizes, confirming a denser microstructure

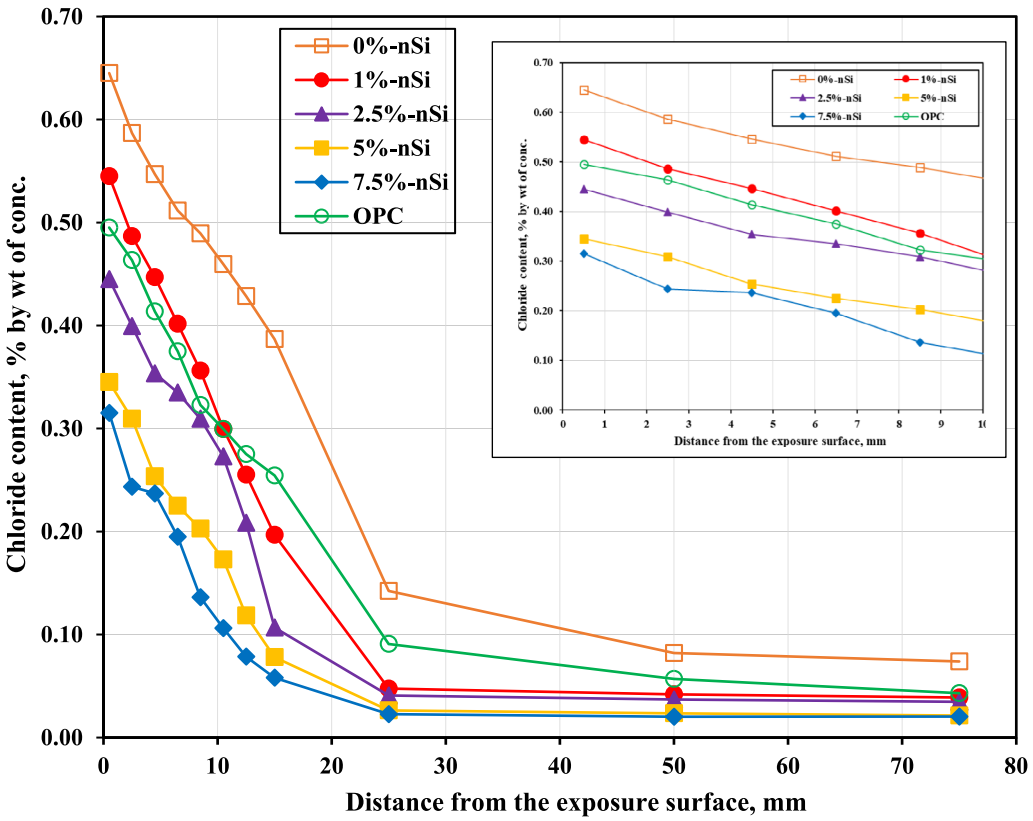

Fig. 9 Chloride profiles of various concrete mixes after 35 days of exposure

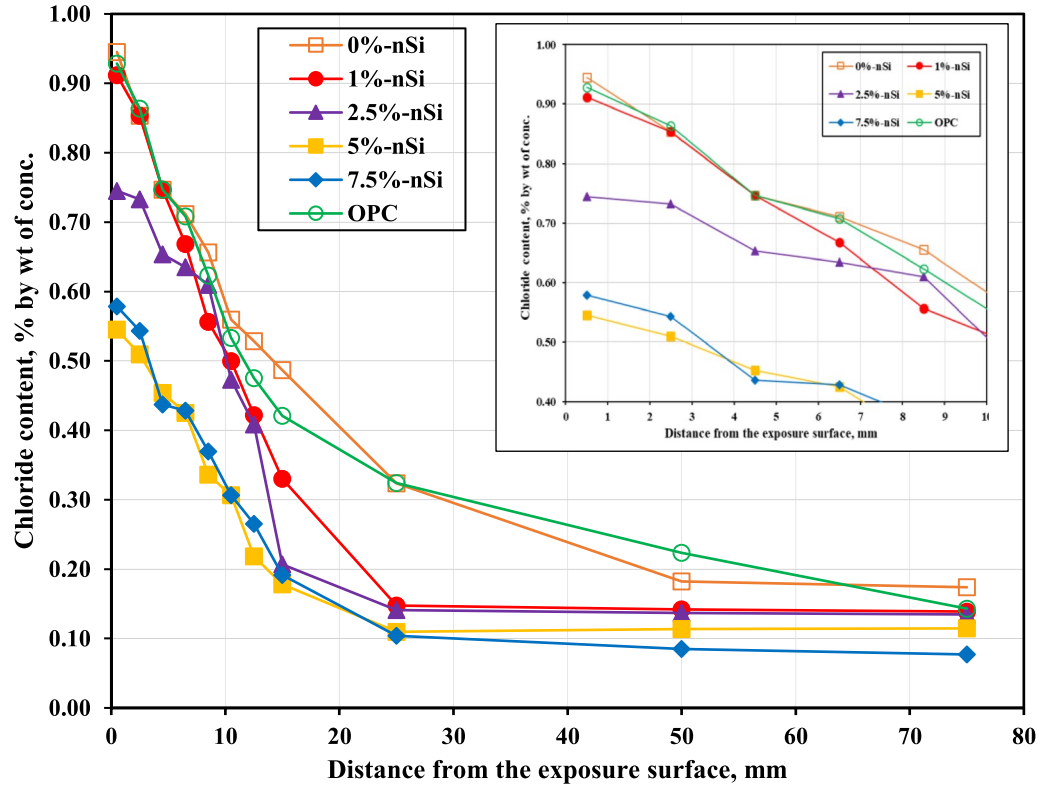

Fig. 10 Chloride profiles of various concrete mixes after 90 days of exposure

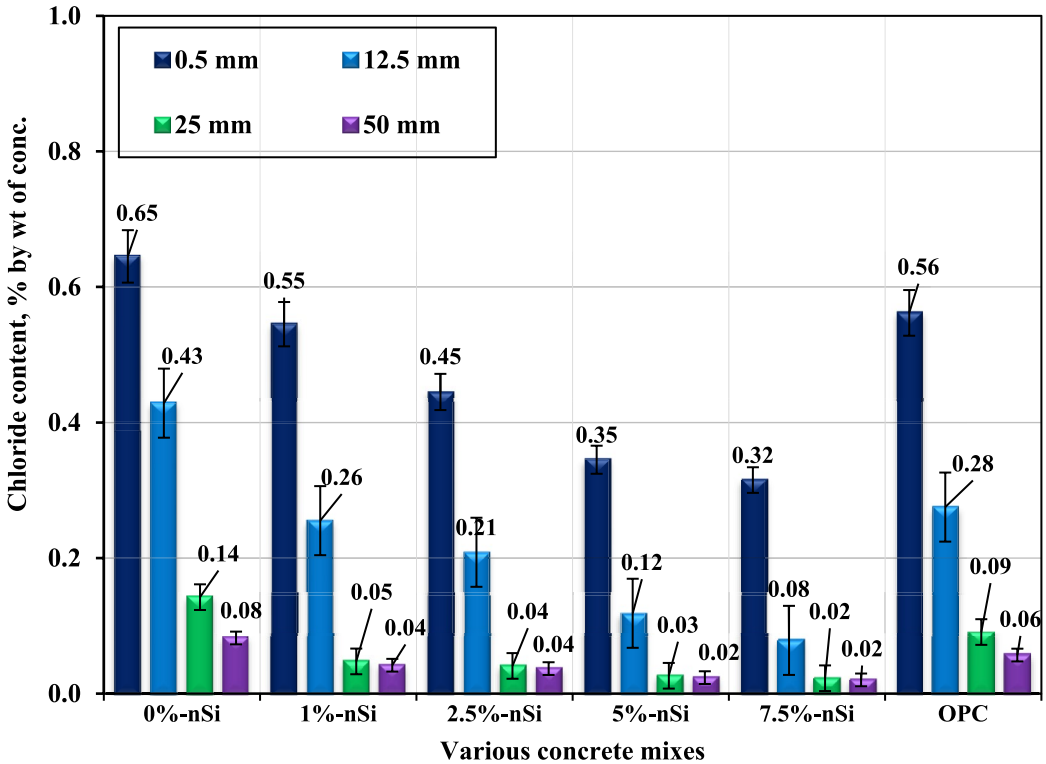

Fig. 11 Chloride content in cover concrete after 35 days of exposure

in high nSi mixes. In addition, cumulative porosity values decrease with increasing nSi, particularly in the mesopore range (10–100 nm), which is most relevant to chloride ion transport. Further discussion is provided in the subsequent sections.

After 90 days of exposure at a depth of 25 mm, the chloride content was approximately 0.32, 0.11, 0.11, 0.08, and 0.08% by weight of concrete in the AAC mixes modified with 0, 1, 2.5, 5, and 7.5% nSi, respectively. At a depth of 50 mm, these values were 0.18, 0.11, 0.10, 0.09, and 0.06 percent, respectively (Fig. 12). Various governing codes specify different chloride threshold values. Among these, ACI 318 (ACI, 2014) provides a limit of acid-soluble chloride concentration of 0.1% and 0.2% by weight of binder in wet and dry conditions, respectively, which corresponds to 0.5% and 1% by weight of concrete. Hence, the chloride concentration values measured for various mixes were lower than the limits, particularly at a depth of 25 and 50 mm corresponding to the concrete cover in normal and marine exposure conditions, respectively. The chloride concentrations in the AAC mixes incorporating nSi were significantly lower than the control AAC and OPC concrete. It appeared from the results that the pathways available for chloride penetrability is reduced with the nSi-modified mixtures, particularly those having 5.0 and 7.5%-nSi at both exposure durations, due to the microstructural denseness (fewer and smaller pores) contributed by the nanomaterials. This indicates that, beside OPC-based mixes, the AAC mixes displayed excellent resistance to chloride penetration, as the dosage of nSi increases.

Compared to traditional materials, the incorporation of GVP and nSi significantly enhances the pore structure and reduces chloride penetration. Mehta and Siddique reviewed sustainable geopolymer concrete using fly ash, GGBFS, and nSi, but the use of GVP as a precursor remains underexplored. This study demonstrates that nSi-modified mixes with 5.0% and 7.5% nSi exhibit superior chloride resistance, outperforming previous formulations reported in the literature (Mehta & Siddique, 2018). The study's findings are supported by empirical data showing a 30% reduction in chloride diffusion coefficients compared to control mixes. Weise et al. discussed the heat of reaction in alkali-activated binders, emphasizing the importance of nano-scale interactions in refining pore structures and improving durability (Weise et al., 2024).

There has been limited research on chloride ion diffusion in AABs. Studies (Ibrahim et al., 2020; Runci & Serdar, 2022; Zhou et al., 2024) investigated fly ash-based AAC with GGBFS, incorporating varying percentages of nSi to enhance microstructural properties and durability. Increasing the GGBFS content in fly ash-based AAC has been reported to reduce chloride ion concentration when exposed to a 2.826 M NaCl solution (Tennakoon et al., 2017). Tennakoon et al. (2017) found that in an

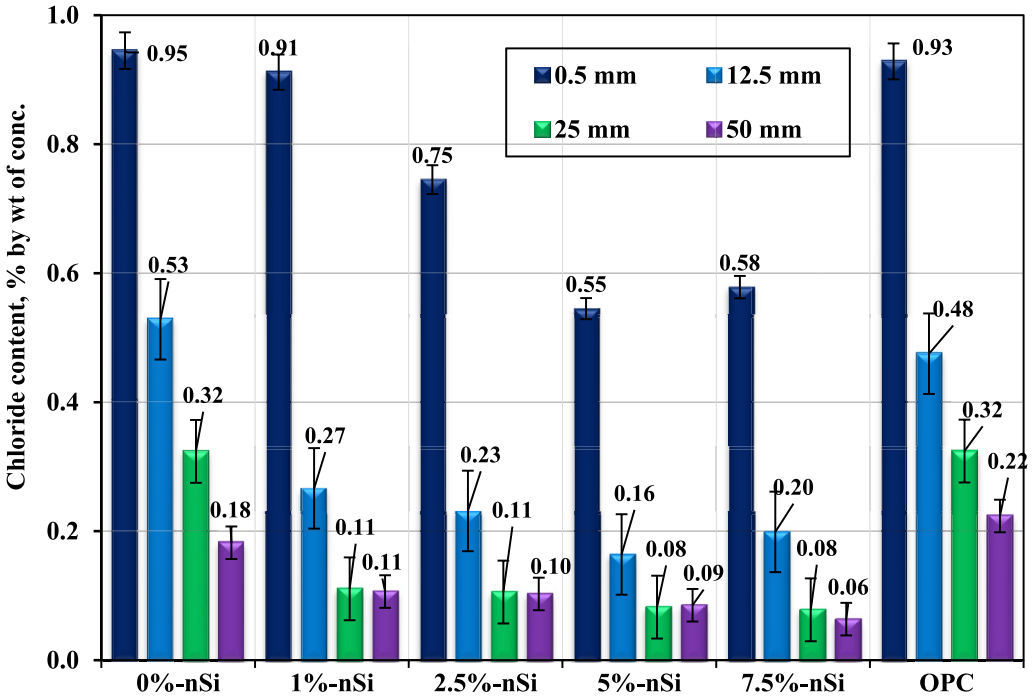

Fig. 12 Chloride content in cover concrete after 90 days of exposure

alkali-activated mix with a 50%–50% fly ash and GGBFS ratio, the chloride content was approximately 0.88% at 1 mm from the exposure surface and decreased to 0.007% at a depth of 40 mm. Similarly, Zhang et al. (2020) examined chloride ion diffusion in binary mixes containing fly ash and GGBFS. Their findings showed that increasing GGBFS content enhanced resistance to chloride penetration, with free chloride ion concentrations ranging between 0.1% and 0.6% after 90 days and 0.1% and 0.7% after 180 days of exposure to a 3.5% NaCl solution. In both cases, the chloride concentration reached its minimum at approximately 18 mm from the exposure surface and peaked at around 2 mm. According to the latest literature, no studies have specifically examined the chloride diffusion properties of GVP-based AABs, particularly those incorporating nSi.

Comparing the results of the current study with existing literature is not appropriate due to the prior studies mainly focusing on the use of fly ash either as a primary precursor material or in combination with GGBFS. Nonetheless, the general trend observed in chloride profiles in the present study aligns well with prior research, particularly in low-Ca binders. The fly ash-based mixes containing about 10% GGBFS agreed well with the GVP-based control mixture of the current study, while mixes having nSi in the GVP-based AAB outperformed the mixes prepared with greater GGBFS content in the previous studies. The apparent chloride diffusion coefficient was determined in accordance with Fick's second law of diffusion using a non-regression analytic technique applied to the study data. The average apparent coefficient of chloride diffusion (D) of various mixes is displayed in Fig. 13. The D value of control AAC without nSi was found to be about 18.40×10^{-12} m^2/s, whereas it was marginally lower in the OPC-based concrete (17.60×10^{-12} m^2/s). Though there was a nearly proportional decrease in the D values with the increase in the addition of nSi. It was about 60% in the 5.0% and 7.5%-nSi modified AAC compared to the control mix. Incorporation of nSi in the cementitious binder is known to draw more cementitious precipitates, along with the physical influence on the pore structure (Tabish et al., 2023; Yang et al., 2021). These factors tend to decrease the diffusion of ions into the binders. This may have been the reason for the significant enhancement in the performance of nSi-admixed AAC in this study. A more detailed analysis of factors influencing chloride diffusion in the AAC is presented in the discussion section of this manuscript.

A review of literature on low-Ca AABs exhibited a higher magnitude of chloride diffusion coefficient. For instance, the data reported by Noushini et al. (2021) for mixes containing less than 25% GGBFS have shown an apparent diffusion coefficient of more than 30×10^{-12}

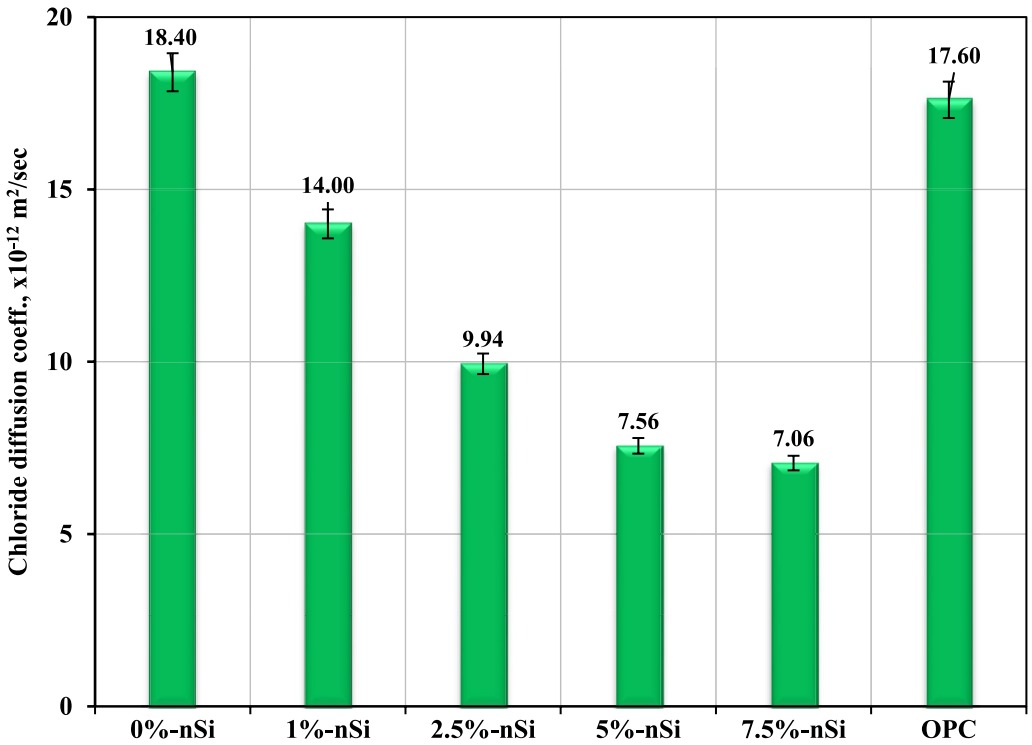

Fig. 13 Chloride content in cover concrete of various concrete mixes after 90 days of exposure

m^2/s. There was a significant decrease in the chloride diffusion coefficient of concrete mixes containing a considerable quantity of GGBFS, though they were cured at room temperature. Some of these mixes were reported to have a coefficient of chloride diffusion lower than 5×10^{-12} m^2/s. In the current study, similar order values of the coefficient of chloride diffusion were obtained for the mixes having nSi ≥ 5%. Elsewhere (Jin et al., 2022), the free chloride diffusion coefficient was also decreased with increasing the GGBFS content. It was in the range of 0.25 to 1.75×10^{-12} m^2/s in the mixes containing 30 to 100% GGBFS. These values are lower than those obtained in the current study as well as those reported by Noushini et al. (Noushini et al., 2021). The lower coefficient may be attributed to a couple of reasons; the NaCl solution to which the samples were exposed had a concentration of about 3.5%, which was lower than the concentration specified in ASTM C1556 (ASTM International, 2022), and the chloride concentrations determined were water-soluble, which does not include physically and chemically bound chloride ions. Additionally, Tennakoon et al. (2017) reported a decrease in the coefficient of chloride diffusion with the increase in GGBFS content, and a mixture of 50% fly ash and 50% GGBFS was reported to have a coefficient of about 2.38×10^{-12} m^2/s. However, the gel chemistry also influences the chloride diffusion. The cited examples have used high-Ca precursor materials where C–A–S–H is a dominant reaction product. In the present study, low-Ca precursor was used in the form of GVP wherein N–A–S–H is a predominant gel that binds aggregates. Low-Ca AACs generally exhibit higher chloride diffusivity than GGBFS-based AACs due to their inherently higher porosity and reduced chloride-binding capacity. However, the incorporation of nano-silica significantly refined the pore network thereby increased tortuosity and reduced connectivity, which in turn lowers the effective chloride diffusion coefficient. This has been discussed in great detail in the subsequent sections. However, it is worth mentioning that the long-term pore structure refinement and chloride penetration resistance of GVP-AAC mixes incorporating GGBFS require further investigation. Understanding these long-term effects is crucial for assessing the durability performance of nSi-modified AACs and their potential synergy with GGBFS.

3.2 Pore Structure and Pore Connectivity

Fig. 14a and b illustrates the cumulative porosity of various concrete mixes prepared in the study, including conventional OPC-based concrete. Fig. 15 shows the pore size distribution of the GVP-AAC incorporating nSi. The cumulative porosity curves in Fig. 14a and b demonstrates that the control mix (0%-nSi) exhibits the highest cumulative porosity across all pore diameters, indicating a relatively more porous structure. As the nSi content increases, there is a noticeable reduction in cumulative porosity, particularly in the smaller pore ranges (1 to 100 nm). This suggests that nSi effectively fills and refines the pore structure, leading to a denser matrix. As curing progresses, cumulative porosity decreases, as shown by comparing Fig. 14a and b. After 28 days, all mixes exhibit higher porosity than after 90 days, indicating ongoing densification and pore refinement with curing time. For instance, the mix with 5% nSi shows a reduction in cumulative porosity from around 11% at 28 days to approximately 8% at 90 days, highlighting the significant impact of prolonged curing on pore structure refinement. In the same vein, higher nSi contents (5% and 7.5%) demonstrate the lowest cumulative porosity, suggesting that increased nSi dosages contribute to greater pore filling and a more compact matrix. The 7.5%-nSi mix shows cumulative porosity decreasing from about 10% at 28 days to around 7% at 90 days, indicating an effective reduction in porosity with higher nSi content.

The pore size distribution in Fig. 15 reveals that the majority of the porosity reduction occurs in larger pores (> 100 nm). The control mix (0% nSi) has a higher proportion of larger pores compared to nSi-modified mixes. With increasing nSi content, there is a marked reduction in larger pores, accompanied by an increase in finer pores (< 10 nm). This indicates that nSi promotes the formation of smaller, more evenly distributed pores, contributing to overall matrix densification. Medium pores (10 to 100 nm and 100 to 1000 nm) also decrease with increasing nSi content. The mix with 2.5%-nSi shows a reduction in medium pores compared to the control, and this trend continues with higher nSi contents. This reduction in medium pores further supports the hypothesis that nSi contributes to pore refinement and the formation of a denser microstructure. Total porosity in the control AAC is over 18% after 28 days of curing and decreases slightly after 90 days. In contrast, nSi-modified mixes show a significant reduction in total porosity with increasing nSi content. For example, the cumulative pore volume in the 5.0% and 7.5%-nSi mixes is below 12% after 28 days of curing and decreases to around 10% at 90 days. These values indicate a significant influence on pore structure refinement with prolonged curing periods. All these showed that the addition of nSi significantly refines the pore structure of GVP-AAC, reducing both cumulative porosity and the size of medium and larger pores, while increasing the proportion of finer pores. Due to the refinement in the pore structure particularly in the 5% and 7.5% nSi modified concrete, there was significant

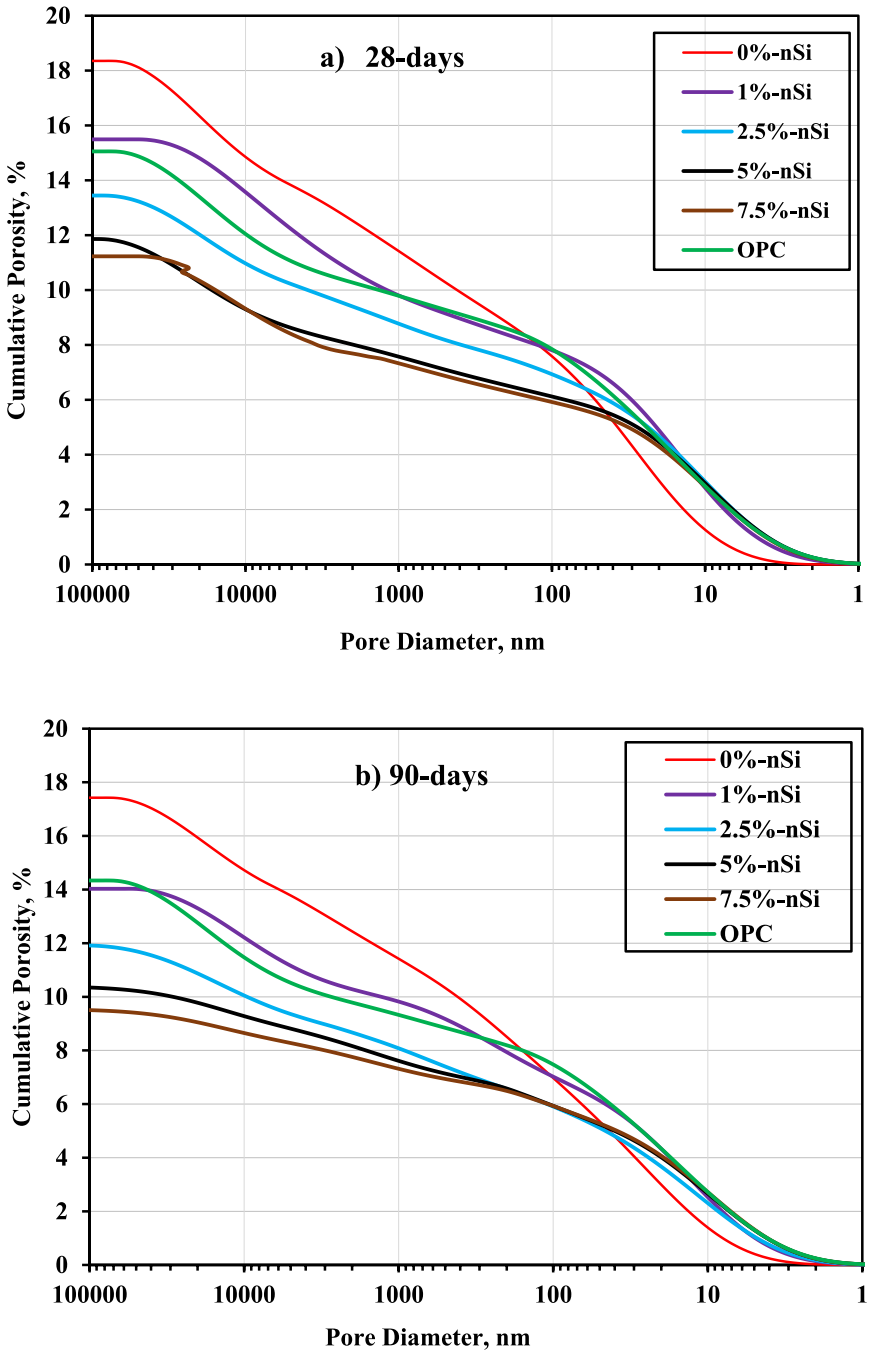

Fig. 14 Cumulative porosity of various concrete mixes: **a** 28 days; **b** 90 days of curing

reduction in the chloride ion penetration. For instance, there was an 80% to over 90% decrease in chloride concentration as the depth increased from 0.5 mm to 25 mm. This leads to a denser and less permeable matrix, enhancing the overall durability and performance of the concrete. Prolonged curing further enhances these effects, indicating the importance of both nSi content and curing time in optimizing the pore structure of GVP-AAC.

Figs. 16, 17, 18, 19, 20, 21 show T_2-store-T_2 maps of various alkali-activated mixes prepared in the current study along with a typical conventional OPC-based concrete. Typically, T_2-store-T_2 maps reveal three distinct peaks: (i) an intense peak along the diagonal (well

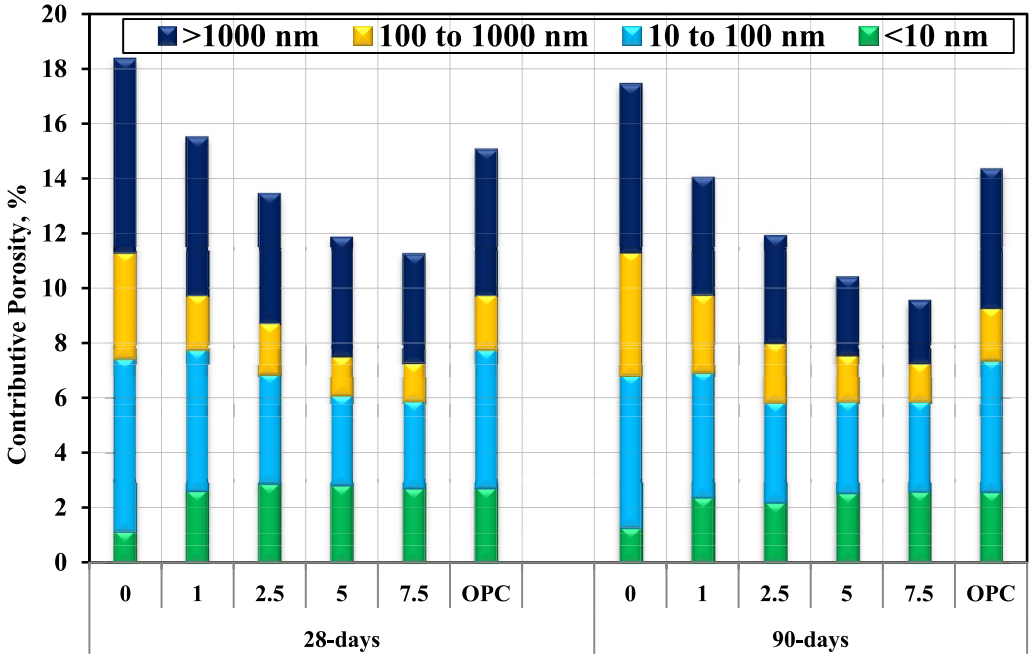

Fig. 15 Pore size distribution of various concrete mixtures

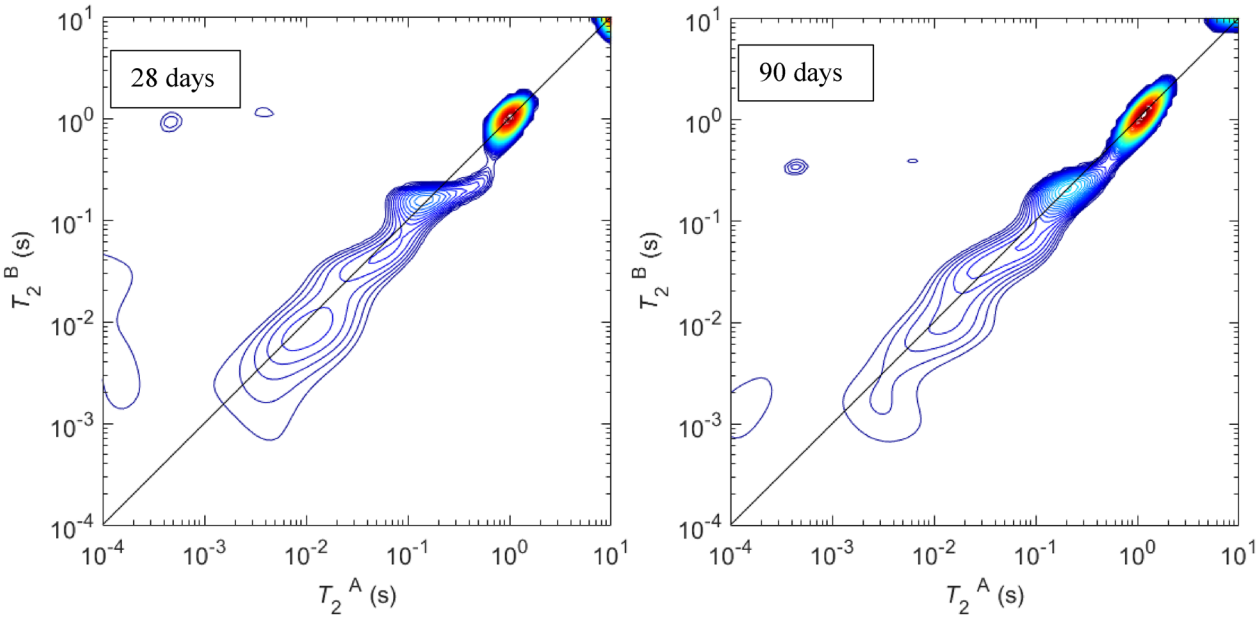

Fig. 16 Pore connectivity at 28 and 90 days of curing in 0%-nSi samples

centered on $T_2 = T_2$) generally forms due to large pores within the binder structure during the early polymerization process of cementitious binders. This is identified due to the fact that the time taken to probe the larger pores would be longer compared to the smaller ones; (ii) an extended peak along the diagonal represents smaller pores wherein no exchange of NMR signals occurs, indicating their lack of connectivity; and (iii) off-diagonal peaks denote signal exchange, which imply some level of pore interconnectivity (Valori, 2009). In this study, all figures reveal a prominent peak along the diagonal, typically at around 1 s,

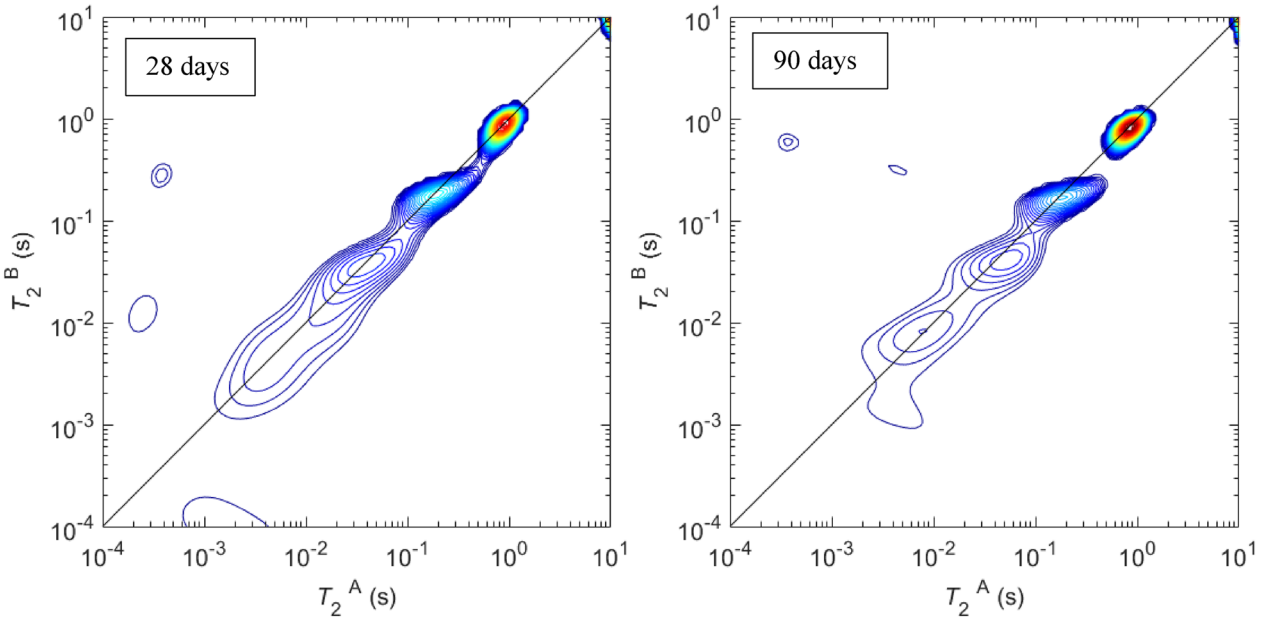

Fig. 17 Pore connectivity at 28 and 90 days of curing in 1.0%-nSi samples

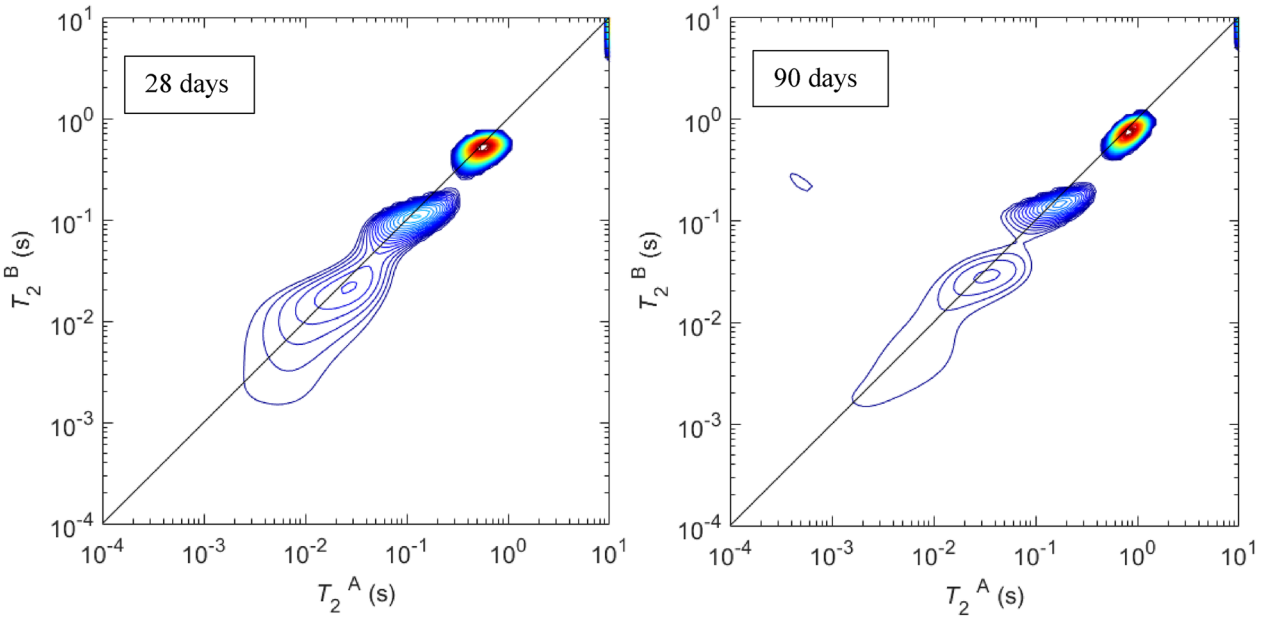

Fig. 18 Pore connectivity at 28 and 90 days of curing in 2.5%-nSi samples

corresponding to the maximum probing time for water in the pores. This peak represents larger pores within the binder structure (Korb, 2009). The intensity and extent of this peak diminish with curing age, attributed to the precipitation of reaction products, resulting in pore refinement. Moreover, the intensity and extent of this peak decrease with increasing nSi content in the mixtures. Specifically, AAC mixes without nSi exhibit broadened and visible peaks, while those incorporating 5.0% and 7.5%-nSi display diminished intensities. Additional peaks along the diagonal, spanning from 1 s to 1 ms, denote finer pores with shorter probing times. These peaks exhibit varying widths and intensities, whereas control AAC mixes typically show broader

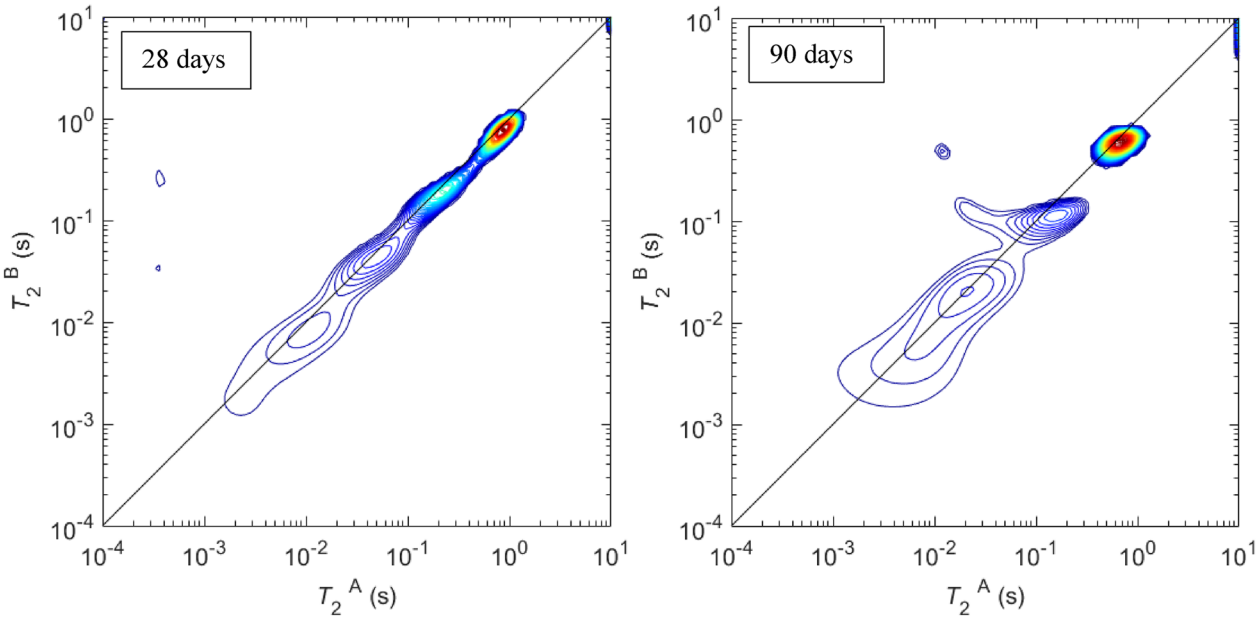

Fig. 19 Pore connectivity at 28 and 90 days of curing in 5.0%-nSi samples

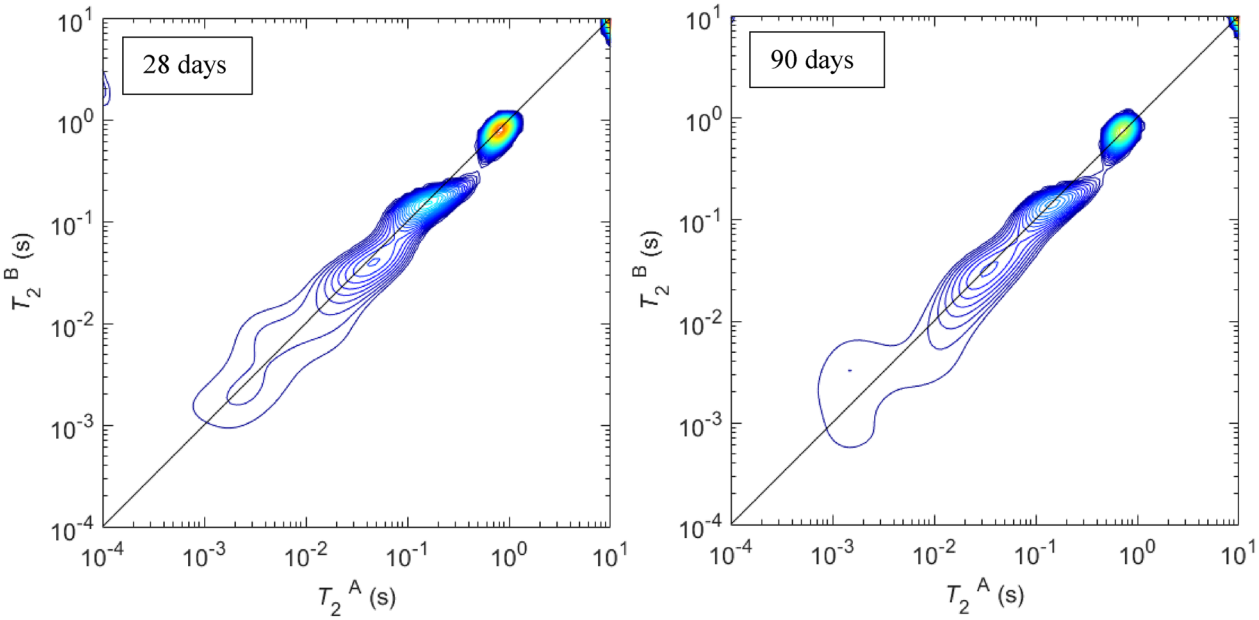

Fig. 20 Pore connectivity at 28 and 90 days of curing in 7.5%-nSi samples

and more pronounced features. However, the addition of nSi correlates with reduced intensity and stretch of these peaks, particularly evident in mixes with higher nSi dosages (> 5.0%).

On the other hand, the off-diagonal peaks indicate that there is some exchange of signals, implying pore connectivity (McDonald et al., 2005, 2007). There have been small peaks noticeable above and below the diagonal in the AAC mix prepared without nSi and in the mixes prepared with 1.0%, 2.5% and 5.0%-nSi. However, the extent of these peaks was the least in the cases of 2.5% and 5.0%. There has been no peak located above or below the diagonal in the mix having 7.5%-nSi. This means that there are no interconnected pores in this matrix (Li et al.,

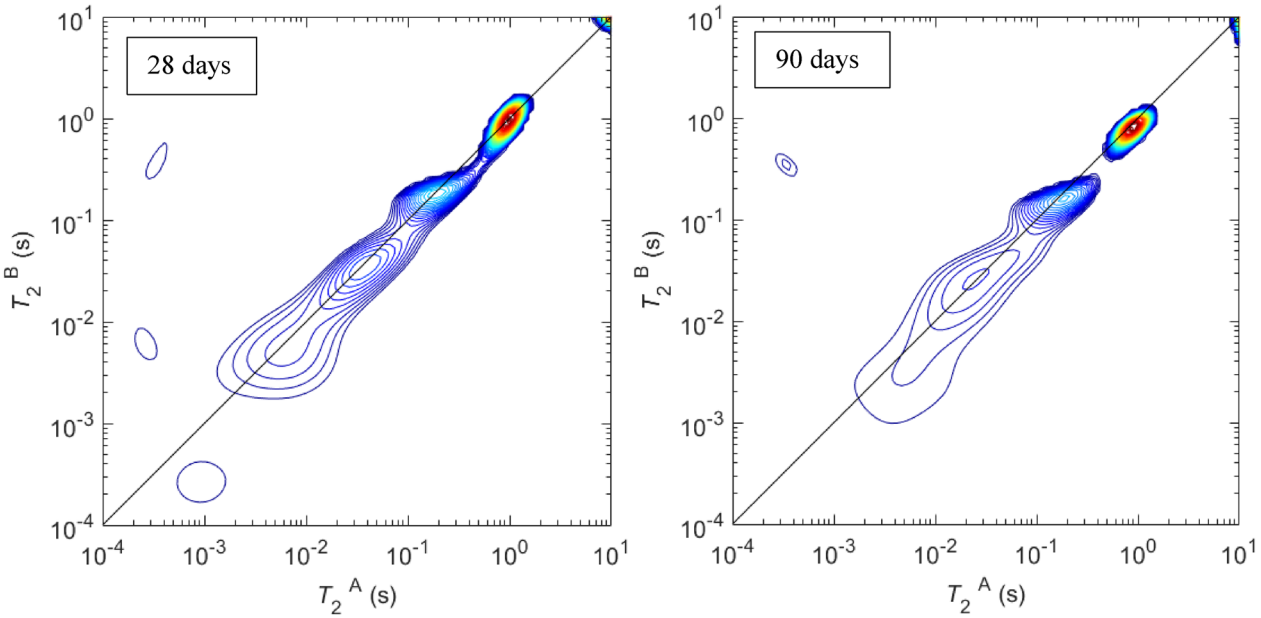

Fig. 21 Pore connectivity at 28 and 90 days of curing in OPC concrete

2021). Further, the pore connectivity was also minimal in the cases of 2.5% and 5.0%-nSi modified concrete. Pore connectivity in cementitious binders critically influences the diffusivity and tortuosity of concrete. Unconnected pores are advantageous as they impede the ingress of deleterious chloride and sulfate ions, which can compromise the structural integrity of concrete. Chloride ions facilitate the corrosion of steel reinforcement bars by disrupting their passive oxide layer, while sulfate ions induce the decalcification of the cementitious matrix, leading to the deterioration of binder gels. Reducing pore connectivity in cementitious binders is essential for enhancing the durability of reinforced concrete structures, particularly in aggressive environments rich in chloride and sulfate ions. This reduction minimizes ion penetration, thereby preserving the structural integrity and extending the service life of concrete. Enhancing pore structure by minimizing connectivity effectively protects concrete from ion-induced degradation, ensuring its reliability and longevity in harsh conditions.

3.3 Mechanistic Insights into Microstructure and Corrosion Resistance

The degree of chemical reaction and the mineralogical characteristics of the binder are crucial factors that impart strength to the pore structure. The SEM analysis (Fig. 22) of the AAPs synthesized shows that the degree of polymerization was enhanced due to the addition of small amounts of nSi. Generally, the gel pores were evident in the AAP prepared without nSi. However, the uniformity of the binder structure improved with the incorporation of nSi. The plate-like structures were commonly evident in micrographs. The connectivity between the plates improved with the increase in nSi content. The uniformity and compactness were superior in the 5.0% and 7.5%-nSi modified AAP. However, in the SEM image of the 7.5%-nSi incorporated specimen, some agglomerations of particles were observed. The observed reduction in T_2 peak range and intensity in 5.0% and 7.5% nSi samples is a direct consequence of enhanced microstructural densification and pore connectivity reduction induced by nano-silica incorporation. The shorter T_2 relaxation times indicate a shift toward smaller, more isolated pores, suggesting that nano-silica significantly refines the pore network by promoting additional gel formation and densification of the binder matrix. As nSi provides a highly reactive source of amorphous silica, it accelerates the polymerization of aluminosilicate gels (N–A–S–H), leading to a denser pore structure with fewer interconnected voids. This increased tortuosity and reduction in large, percolating pores directly impact chloride ion transport, as the diffusion pathways become more restricted, thereby reducing effective chloride permeability.

The compressive strength of the various concrete mixes was also determined, as shown in Fig. 23. The results of compressive strength were well correlated with the morphology of the specimens. For instance, the incorporation of about 2.5%-nSi resulted in a compressive strength equal to that of OPC-based concrete after about 90 days

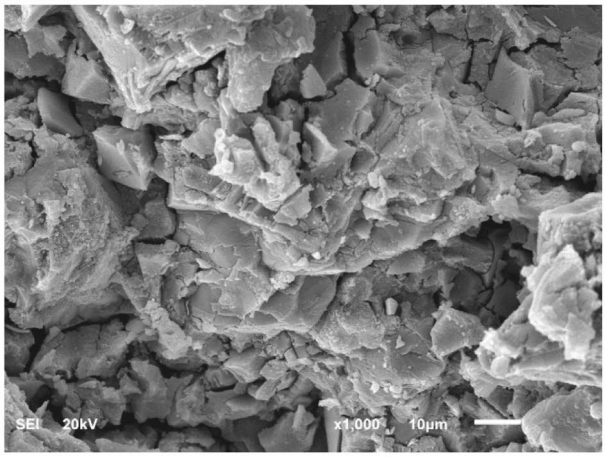

(a) **0.0%-nSi**

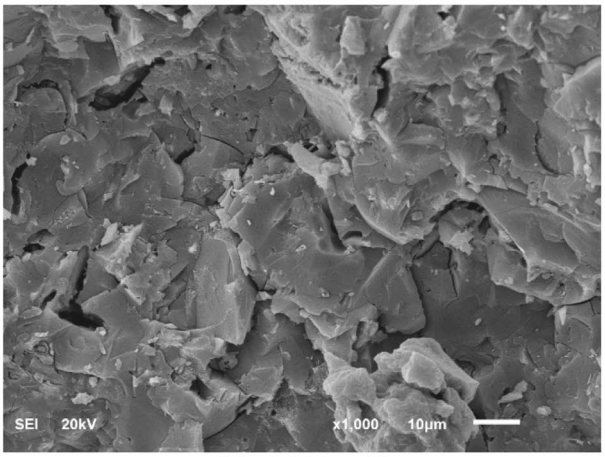

(b) **1.0%-nSi**

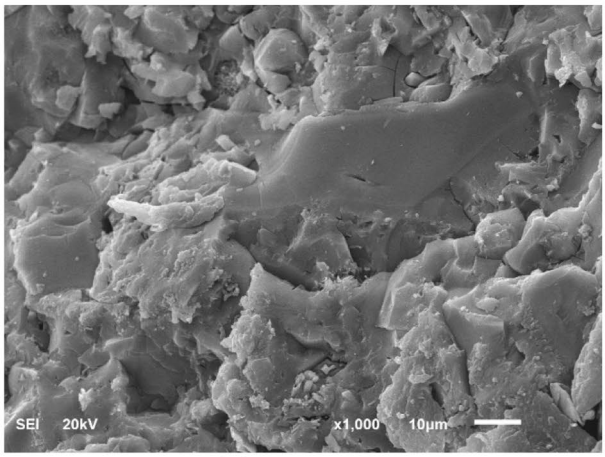

(c) **2.5%-nSi**

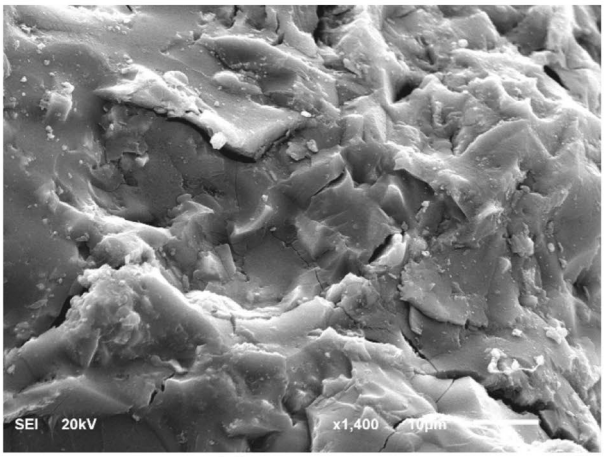

(d) **5.0%-nSi**

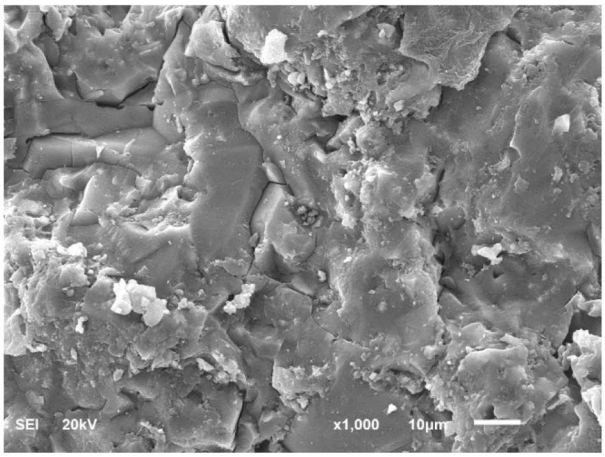

(e) **7.5%-nSi**

Fig. 22 Micrographs of different mixes after 180 days of curing

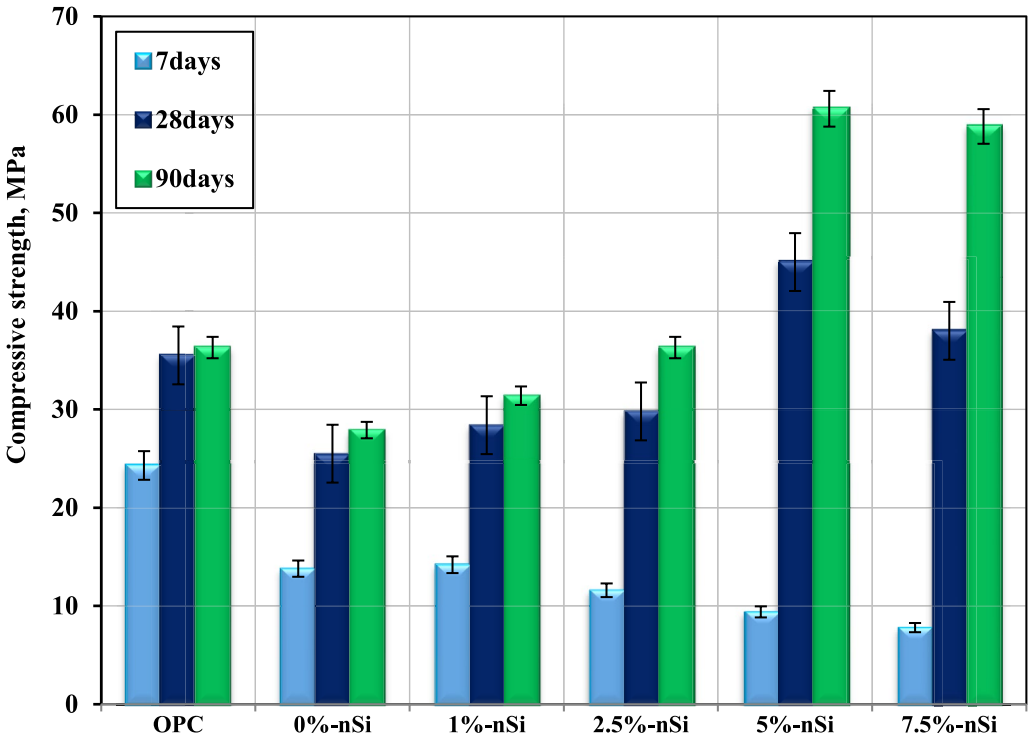

Fig. 23 Compressive strength in various concrete mixtures

of room temperature curing. However, about 60 MPa was recorded in the AAC mix prepared with 5.0%-nSi or more, which shows that there has been more than 60% improvement in the strength compared to OPC concrete. AlTawaiha et al. (2023) demonstrated that nSi incorporation significantly enhances compressive strength and reduces porosity in cement composites, supporting the selected dosage range in this study. Similarly, Dheyaaldin et al. (2022) reported that specific nSi levels improved both the mechanical and durability properties of fiber-reinforced alkali-activated mortars.

As discussed in the preceding sections, the pore connectivity of AAC incorporating nSi was the lowest. The finer pores having a pore diameter less than 10 nm were more in the nSi-modified concrete, and the larger pores having a pore diameter greater than 1000 nm were less, particularly in the AAC mixes having 2.5% or more nSi. These results show that there has been a superior degree of dissolution of the precursors and polymerization in these mixes. Due to these physical characteristics of the binder, the chloride permeability and chloride migration coefficient were lower in the nSi-modified concrete compared to the AAC mix prepared without nSi. Particularly, the 2.5%-nSi or above showed better results. Table 3 shows the rapid chloride permeability and chloride migration coefficients of various concrete mixes.

Table 3 RCPT and migration coefficient of various concrete mixes

Legend	Chloride permeability, Coulombs		Chloride migration coefficient, D_{nssm}, m^2/s ($\times 10^{-12}$)	
	28 days	90 days	28 days	90 days
0%nSi	579	551	16.68	12.82
1%nSi	549	527	14.67	12.63
2.5%nSi	479	456	11.74	10.52
5%nSi	348	327	8.70	7.83
7.5%nSi	343	322	6.93	6.22
OPC	337	323	12.43	10.44

The E_{corr} and I_{corr} values of the steel embedded in various concrete specimens are shown in Figs. 24 and 25, respectively. The nSi-modified mixes exhibited lower negative corrosion potentials on the steel as well as corrosion current density. The E_{corr} values were more negative since the beginning of the exposure, mainly due to the built-in alkalis in the AAC. Generally, the higher E_{corr} and I_{corr} values recorded in AAC compared to OPC concrete are due to the reducing environment around the steel surface caused by high sulfide concentrations, lower pH, and lack of oxygen, which differ from the conditions found in OPC concrete (Ibrahim et al., 2020; Mangat

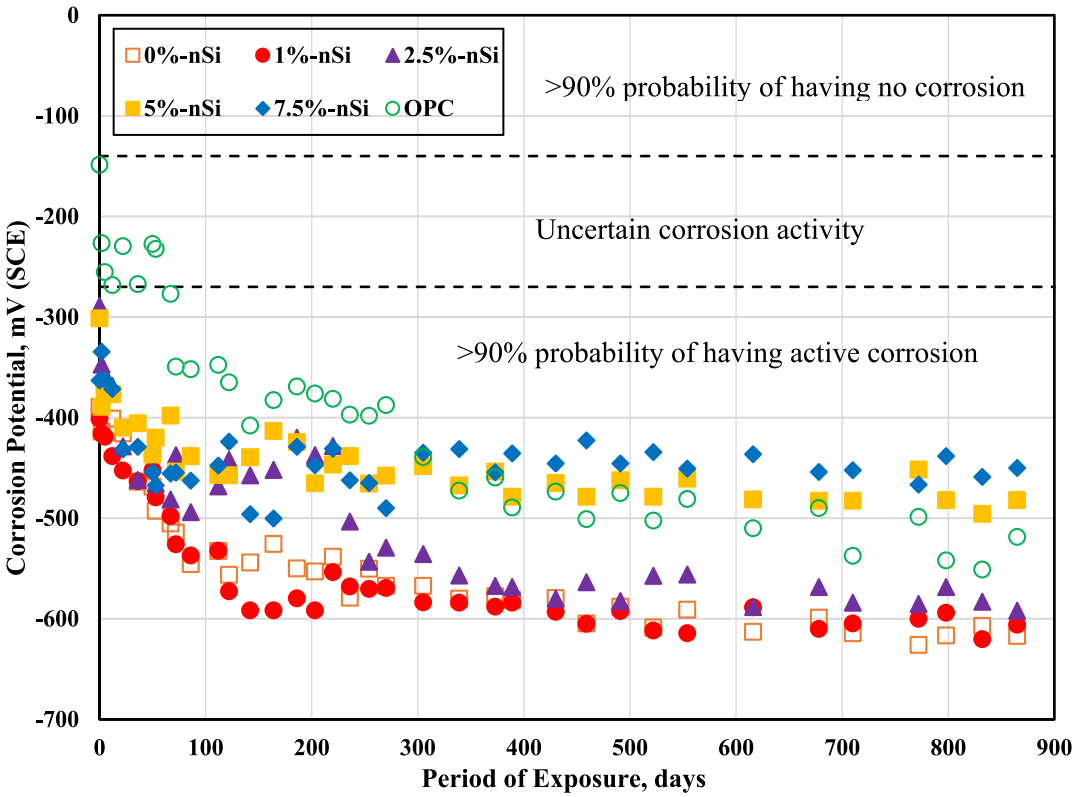

Fig. 24 Variation in corrosion potentials (E_{corr})

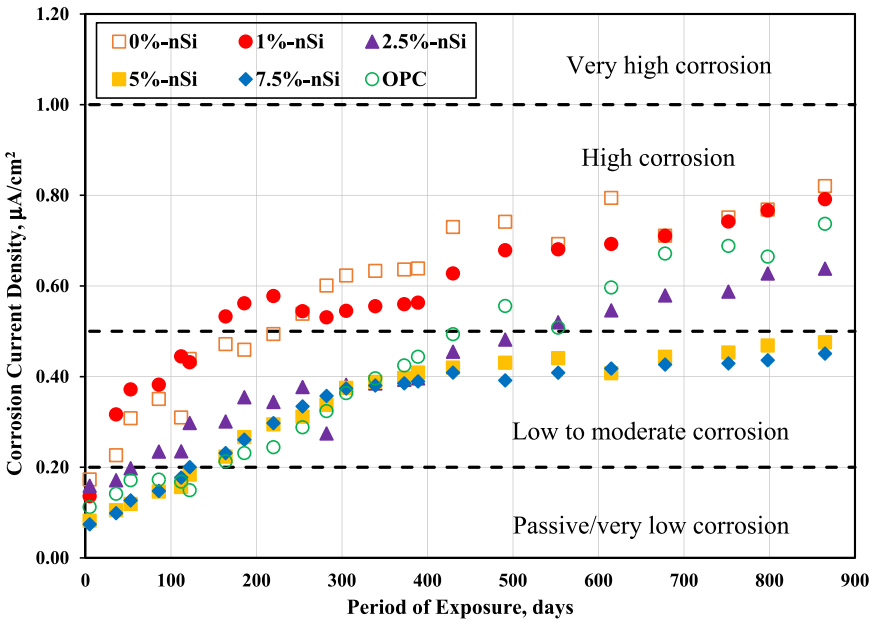

Fig. 25 Variation in corrosion current density (I_{corr})

et al., 2021). High alkalinity from the activators accelerates corrosion processes, and the varied chloride permeability and microstructural differences, such as higher porosity and different hydration products, also contribute to the increased corrosion activity in AAB (Mundra et al., 2017).

However, among the various AAC mixtures evaluated, the nSi-modified concrete demonstrated superior electrochemical performance, as evidenced by the lowest corrosion potential (E_{corr}) and corrosion current density (I_{corr}) observed on the steel reinforcement, as illustrated in Figs. 24 and 25. This enhanced performance is primarily attributed to the significant microstructural properties improvement of the nSi-modified mixes, which resulted in markedly reduced chloride ingress. The reduced chloride diffusion in the nSi-modified AAC is a critical factor in mitigating the initiation and propagation of corrosion activities. This observation aligns with the results of the pore structure and SEM analyses, which revealed a denser and more impermeable microstructure in the nSi-modified AAC. The microstructural characterization indicated a reduction in pore size, pore distribution and connectivity, effectively impeding the diffusion pathways for chlorides and other aggressive ions. These microstructural enhancements create a robust barrier against chloride ingress, thereby providing enhanced protection to the embedded steel rebar. The long-term stability of the electrochemical properties of the nSi-modified AAC was further corroborated by the consistent E_{corr} and I_{corr} values, even after extended exposure of up to 865 days in a chloride-laden environment. These modifications not only enhance the material's resistance to chloride-induced corrosion, but also improve the overall durability and longevity of reinforced concrete structures in aggressive environmental conditions. The comprehensive analysis of both short-term and long-term performance metrics firmly establishes nSi-modified AAC as a superior alternative to conventional Portland cement concrete in mitigating corrosion risks and enhancing structural durability.

3.4 LCA Study

Fig. 26a shows the LCA results of all mixes. The CO_2 emissions of the GVP-based alkali-activated mixes vary from 136.6 kg·CO_2/m^3 (M-0) to 159.3 kg·CO_2/m^3 (M-4), while the OPC-based reference mix (M-OPC) emits significantly more at 341.9 kg·CO_2/m^3. This equates to a 53% to 60% reduction in CO_2 emissions for the GVP-based mixes compared to the conventional OPC mix, which is a substantial improvement in environmental performance. Among the GVP-based mixes, the one with no nSi (M-0) has the lowest GWP, suggesting that increasing nSi content directly impacts the carbon footprint. M-4, with the highest nSi dosage (7.5%), has the largest CO_2 emissions due to the contribution from nSi production. Despite the higher emissions associated with nSi, all GVP-based mixes still present a marked reduction in GWP compared to the OPC mix, emphasizing the potential for carbon footprint reduction. This result is promising for sustainable construction, as GVP-based alkali-activated systems can provide a viable alternative to traditional OPC, significantly reducing environmental impacts

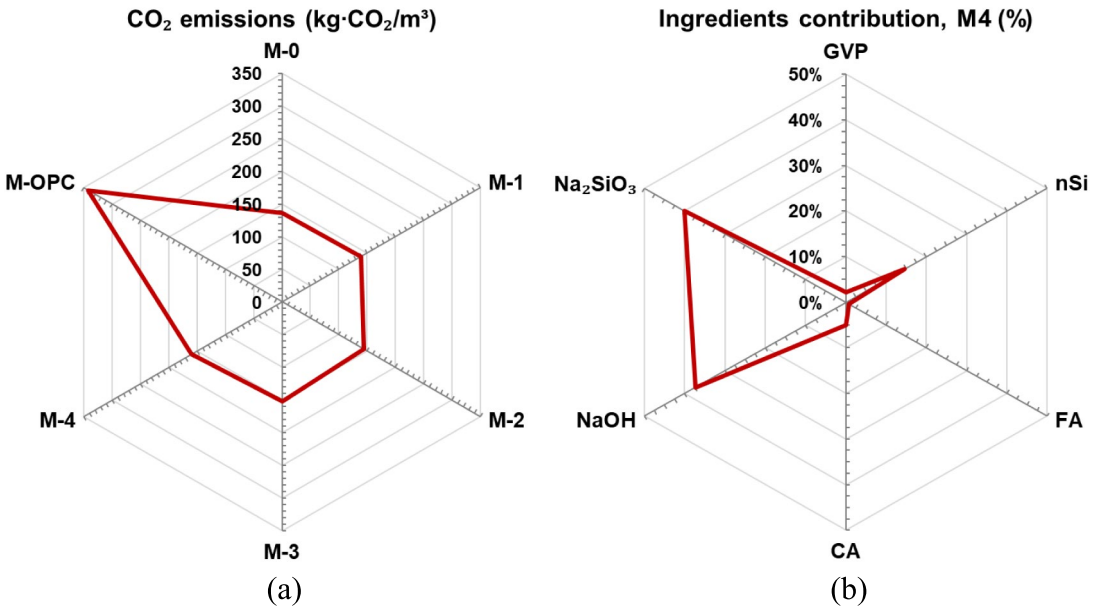

Fig. 26 LCA results: **a** CO_2 emissions of all mixes; and **b** contribution of the ingredients of a typical mix (M4)

while maintaining suitable performance. In comparison with the previous studies, several researchers have reported about 45% reductions in GWP for alternative cementitious materials, including natural pozzolan-based alkali-activated concrete and fly ash-based geopolymer concrete (Habert et al., 2011; Robayo-Salazar et al., 2018). These findings align well with the GWP reductions observed in the GVP-based alkali-activated mixes in this study, which achieved a reduction of 53% to 60%.

In terms of the sources of CO_2 emissions within the GVP-based mixes, the most significant contributors are NaOH and Na_2SiO_3, which together account for over 90% of the total emissions across all mixes, as shown in Fig. 26b. This is due to their high-energy manufacturing processes, particularly the synthesis of sodium hydroxide and sodium silicate, which are crucial activators in alkali-activated systems (Ouellet-Plamondon & Habert, 2015). Therefore, it is worth emphasizing the importance of utilizing more sustainable activators derived from waste or by-products and produced locally to mitigate environmental impact (Kumar et al., 2023). Replacing NaOH with KOH can reduce carbon emissions, as KOH production has a lower energy demand per unit compared to NaOH in certain industrial settings. Additionally, the use of recycled alkaline solutions (e.g., industrial waste-derived sodium silicate or geopolymer precursor leachates) has been explored as a viable approach to minimize emissions associated with virgin activator production (Kumar et al., 2023). In addition, certain industrial by-products are also alkaline in nature, thus may well be explored substituting commercially available energy-intensive alkaline activators such as NaOH and Na_2SiO_3. These strategies align with the circular economy concept and can help further lower the carbon footprint of alkali-activated materials. In contrast, ingredients like GVP and FA contribute minimally to the overall carbon footprint, with GVP emissions ranging from 3.4 to 3.7 $kg{\cdot}CO_2/m^3$ and FA being nearly negligible at 1.4 to 1.5 $kg{\cdot}CO_2/m^3$. The relatively low emissions from GVP, an alternative binder, further highlight its sustainability potential, especially when compared to the high emissions associated with OPC. In fact, the GVP is a naturally occurring material and it requires no pre-treatment or extensive processing (Cabrera-Luna et al., 2020). The performance of these mixes in terms of LCA reflects the balance between leveraging by-products and reducing reliance on energy-intensive activators, paving the way for further optimization in reducing the carbon footprint while achieving high-performance concrete alternatives.

4 Conclusions

This study focused on examining the pore structure of ground volcanic pumice-based alkali-activated concrete exposed to a long-term (865 days) chloride-laden environment using 1H proton NMR relaxometry. Here are the key findings:

1. Significant chloride penetration reduction: We observed a remarkable reduction in chloride penetration, ranging from 80 to 90%, due to the refined pore structure in the nSi-modified mixes as revealed in the NMR results. This improvement was particularly evident in mixes containing 5% and 7.5% nSi during the 35- to 90-day exposure period.
2. Improved porosity and microstructure: The incorporation of nSi reduced total porosity and cumulative pore volume by approximately 10% after extended curing, which indicated a denser microstructure and enhanced durability. SEM analysis further confirmed this, revealing a plate-like structure with improved connectivity, uniformity, and compactness.
3. Detailed NMR relaxometry insights: The study demonstrated the effectiveness of ^{1}H proton NMR relaxometry in analyzing pore structure and connectivity in AAC. The T_2-store-T_2 map showed reduced pore connectivity with increasing nSi content ($\geq$5%), which indicated improved microstructure. NMR relaxometry provides a safer, non-destructive alternative to MIP, supporting its broader use in concrete research.
4. Corrosion resistance: From the beginning of the exposure, the steel reinforcement showed increasingly negative corrosion potentials. However, within the nSi-modified concrete, both the corrosion potential (E_{corr}) and corrosion current density (I_{corr}) of the embedded steel were the lowest, highlighting the superior corrosion resistance of these mixes.
5. Environmental impact: The LCA findings highlights the potential of GVP-based alkali-activated mixes as a sustainable alternative to traditional OPC, significantly reducing CO_2 emissions by 53% to 60% while maintaining performance. This approach not only contributes to lower environmental impacts, but also promotes the utilization of natural materials, paving the way for more eco-friendly construction practices.

In summary, adding nSi to the AAC mix leads to significant improvements in pore structure, reduces chloride ingress, and enhances the corrosion resistance of the embedded steel, thereby increasing the durability of the concrete in harsh environments. This research not only advances our scientific understanding, but also

contributes to building safer and more resilient infrastructure for the future.

Acknowledgements
The authors gratefully acknowledge the support provided by the Applied Research Center for Metrology, Standards and Testing, Research and Innovation, King Fahd University of Petroleum & Minerals, Dhahran, for the reported work.

Author contributions
Corresponding author, Mohammed Ibrahim and Co-Author Ashraf A. Bahraq conducted experimental work, analyzed and prepared results. Prepared draft of manuscript. Co-Author, Babatunde Abiodun Salami, proposed mix design and conducted experiments related to mechanical properties. Partially prepared manuscript. Co-Author, Luai M. Alhems proposed concrete mix composition and raw material characterization. Also, reviewed manuscript. Co-Author, Syed Rizwanullah Hussaini, conducted NMR relaxometry and analyzed the data. Partial writing of manuscript. Co-Author, Muhammad Nasir and Adewale Adewumi, conducted experimental work related to durability of concrete and analyzed data. Partial writing of manuscript. All the authors read and approved the final manuscript.

Funding
The authors declare that no funding was received.

Availability of data and materials
All data are provided in the results section.

Declarations

Ethics approval and consent to participate
Not applicable.

Consent for publication
Authors have approved the manuscript and agree with its submission to *International Journal of Concrete Structures and Materials*.

Competing interests
The authors declare that they have no competing interests.

Received: 4 February 2025 Accepted: 4 April 2025
Published online: 24 July 2025

References

ACI. (2014). ACI 318M-14 Building code requirements for structural concrete.
AlTawaiha, H., Alhomaidat, F., & Eljufout, T. (2023). A review of the effect of nano-silica on the mechanical and durability properties of cementitious composites. *Infrastructures, 8*, 132. https://doi.org/10.3390/INFRASTRUCTURES8090132
ASCE. (2021). America's infrastructure report card 2021,In: American Society of Civil Engineers.
ASTM International. (2022). ASTM C1556: Standard test method for determining the apparent chloride diffusion coefficient of cementitious mixtures by bulk diffusion. https://doi.org/10.1520/C1556-11AR16.
ASTM International. (2022). ASTM C876: Standard test method for corrosion potentials of uncoated reinforcing steel in concrete. 1–8. https://doi.org/10.1520/C0876-15.
Bligh, M. W., d'Eurydice, M. N., Lloyd, R. R., Arns, C. H., & Waite, T. D. (2016). Investigation of early hydration dynamics and microstructural development in ordinary Portland cement using 1H NMR relaxometry and isothermal calorimetry. *Cement and Concrete Research, 83*, 131–139. https://doi.org/10.1016/j.cemconres.2016.01.007
Cabrera-Luna, K., Maldonado-Bandala, E. E., Nieves-Mendoza, D., Castro-Borges, P., & García, J. I. E. (2020). Novel low emissions supersulfated cements of pumice in concrete; mechanical and electrochemical characterization. *Journal of Cleaner Production, 272*, 122520. https://doi.org/10.1016/j.jclepro.2020.122520
Chalid, A. (2021). Effect of the ground granulated blast furnace slag on the pore structure of concrete. *Archives of Civil Engineering, 67*, 203–214. https://doi.org/10.24425/ace.2021.136469
Coates, G. R., Xiao, L., & Prammer, M. G. (1999). *NMR logging, principles and interpretation*. Halliburton Energy Service.
Dheyaaldin, M. H., Mosaberpanah, M. A., & Alzeebaree, R. (2022). Performance of fiber-reinforced alkali-activated mortar with/without nano silica and nano alumina. *Sustainability (Switzerland), 14*, 2527. https://doi.org/10.3390/su14052527
Fairhurst, D., Cosgrove, T., & Prescott, S. W. (2015). Relaxation NMR as a tool to study the dispersion and formulation behavior of nanostructured carbon materials. *Magnetic Resonance in Chemistry, 54*, 521–526. https://doi.org/10.1002/mrc.4218
Fan, X., Zhu, J., & Gao, X. (2025). Sea/coral sand in marine engineered geopolymer composites: Engineering, mechanical, and microstructure properties. *International Journal of Applied Ceramic Technology, 22*, e14874.
Gao, X., Liao, C., Qi, X., & Zhang, Y. (2023). A Scenario simulation of material substitution in the cement industry under the carbon neutral strategy: A case study of Guangdong. *Sustainability, 15*, 5736. https://doi.org/10.3390/su15075736
Golež, M., Serjun, V. Z., Štefančič, M., Rant, D., & Dolenec, S. (2023). Characterisation of 20th Century cementitious materials from selected cultural heritage structures in Slovenia. *Materials, 16*, 6206. https://doi.org/10.3390/ma16186206
Gussoni, M., Greco, F., Bonazzi, F., Vezzoli, A., Botta, D., Dotelli, G., Natali Sora, I., Pelosato, R., & Zetta, L. (2004). 1H NMR spin-spin relaxation and imaging in porous systems: An application to the morphological study of white Portland cement during hydration in the presence of organics. *Magnetic Resononace Imaging, 22*, 877–889. https://doi.org/10.1016/j.mri.2004.01.068
Habert, G., d'Espinose de Lacaillerie, J. B., & Roussel, N. (2011). An environmental evaluation of geopolymer based concrete production: Reviewing current research trends. *Journal of Cleaner Production, 19*, 1229–1238. https://doi.org/10.1016/j.jclepro.2011.03.012
Habert, G., & Ouellet-Plamondon, C. (2016). Recent update on the environmental impact of geopolymers. *RILEM Technical Letters., 1*, 17. https://doi.org/10.21809/rilemtechlett.v1.6
Huang, Z., Wang, J., Bing, L., Qiu, Y., Guo, R., Yu, Y., Ma, M., Niu, L., Tong, D., Andrew, R. M., Friedlingstein, P., Canadell, J. G., Xi, F., & Liu, Z. (2023). Global carbon uptake of cement carbonation accounts 1930–2021. *Earth Syst Sci Data, 15*, 4947–4958. https://doi.org/10.5194/essd-15-4947-2023
Ibrahim, M., Johari, M. A. M., Maslehuddin, M., & Rahman, M. K. (2018). Influence of nano-SiO2 on the strength and microstructure of natural pozzolan based alkali activated concrete. *Construction and Building Materials, 173*, 573–585. https://doi.org/10.1016/j.conbuildmat.2018.04.051
Ibrahim, M., Kalimur Rahman, M., Megat Johari, M. A., Nasir, M., & Adeoluwa Oladapo, E. (2020). Chloride diffusion and chloride-induced corrosion of steel embedded in natural pozzolan-based alkali activated concrete. *Construction and Building Materials, 262*, 120669. https://doi.org/10.1016/J.CONBUILDMAT.2020.120669
Ibrahim, M., & Maslehuddin, M. (2021). An overview of factors influencing the properties of alkali-activated binders. *Journal of Cleaner Production, 286*, 124972. https://doi.org/10.1016/j.jclepro.2020.124972
ISO, Environmental Management - Life Cycle Assessment, Principles and Framework: 14040, International Organization for Standardization, Geneva, 2006.
Jin, H., Li, Z., Zhang, W., Liu, J., Xie, R., Tang, L., & Zhu, J. (2022). Iodide and chloride ions diffusivity, pore characterization and microstructures of concrete incorporating ground granulated blast furnace slag. *Journal of Materials Research and Technology, 16*, 302–321. https://doi.org/10.1016/j.jmrt.2021.11.155
Kenyon, W. E. Petrophysical principles of applications of NMR logging. The Log Analyst. 1997; 38.
Khaiyum, M. Z., Sarker, S., & Kabir, G. (2023). Evaluation of carbon emission factors in the cement industry: An emerging economy context. *Sustainability, 15*, 15407. https://doi.org/10.3390/su152115407
Koleva, D. A., Copuroglu, O., van Breugel, K., Ye, G., & de Wit, J. H. W. (2008). Electrical resistivity and microstructural properties of concrete materials in

conditions of current flow. *Cement and Concrete Composites, 30*, 731–744. https://doi.org/10.1016/j.cemconcomp.2008.04.001

Korb, J.-P. (2009). NMR and nuclear spin relaxation of cement and concrete materials. *Current Opinion Colloid Interface Science, 14*, 192–202. https://doi.org/10.1016/j.cocis.2008.10.004

Kumar, S. S., Rithuparna, R., Senthilkumar, R., & Bahurudeen, A. (2023). Cleaner production of waste-derived alkali activators from industrial and agricultural by-products for sustainable alkali activated binders. *Construction Building Matererial, 391*, 131824. https://doi.org/10.1016/j.conbuildmat.2023.131824

Lambert, J. B., Mazzola, E. P., Ridge, C. Nuclear magnetic resonance spectroscopy : an introduction to principles, applications, and experimental methods, (n.d.) 456. Retrieved June 21, 202, from https://www.wiley.com/en-us/Nuclear+Magnetic+Resonance+Spectroscopy%3A+An+Introduction+to+Principles%2C+Applications%2C+and+Experimental+Methods%2C+2nd+Edition-p-9781119295235

Li, J., Mailhiot, S., Sreenivasan, H., Kantola, A. M., Illikainen, M., Adesanya, E., Kriskova, L., Telkki, V.-V., & Kinnunen, P. (2021). Curing process and pore structure of metakaolin-based geopolymers: Liquid-state 1H NMR investigation. *Cement and Concrete Research, 143*, 106394. https://doi.org/10.1016/j.cemconres.2021.106394

Lübeck, A., Gastaldini, A. L. G., Barin, D. S., & Siqueira, H. C. (2012). Compressive strength and electrical properties of concrete with white Portland cement and blast-furnace slag. *Cement and Concrete Composites, 34*, 392–399. https://doi.org/10.1016/j.cemconcomp.2011.11.017

Ma, H., Tang, S., & Li, Z. (2015). New pore structure assessment methods for cement paste. *Journal of Materials in Civil Engineering*. https://doi.org/10.1061/(asce)mt.1943-5533.0000982

Maddalena, R., Roberts, J. J., & Hamilton, A. (2018). Can Portland cement be replaced by low-carbon alternative materials? A study on the thermal properties and carbon emissions of innovative cements. *Journal Cleaner Production, 186*, 933–942. https://doi.org/10.1016/j.jclepro.2018.02.138

Mangat, P. S., Ojedokun, O. O., & Lambert, P. (2021). Chloride-initiated corrosion in alkali activated reinforced concrete. *Cement and Concrete Composites, 115*, 103823. https://doi.org/10.1016/J.CEMCONCOMP.2020.103823

McCarter, W. J., Chrisp, T. M., & Starrs, G. (1999). The early hydration of alkali-activated slag: Developments in monitoring techniques. *Cement and Concrete Composites, 21*, 277–283. https://doi.org/10.1016/s0958-9465(99)00007-4

McDonald, P. J., Korb, J.-P., Mitchell, J., & Monteilhet, L. (2005). Surface relaxation and chemical exchange in hydrating cement pastes: a two-dimensional NMR relaxation study. *Physical Review E, 72*, 11409. https://doi.org/10.1103/PhysRevE.72.011409

McDonald, P. J., Mitchell, J., Mulheron, M., Aptaker, P. S., Korb, J.-P., & Monteilhet, L. (2007). Two-dimensional correlation relaxometry studies of cement pastes performed using a new one-sided NMR magnet. *Cement and Concrete Research, 37*, 303–309. https://doi.org/10.1016/j.cemconres.2006.01.013

McDonald, P. J., Rodin, V., & Valori, A. (2010). Characterisation of intra- and inter-C–S–H gel pore water in white cement based on an analysis of NMR signal amplitudes as a function of water content. *Cement and Concrete Research., 40*, 1656–1663. https://doi.org/10.1016/j.cemconres.2010.08.003

Mehta, A., & Siddique, R. (2018). Sustainable geopolymer concrete using ground granulated blast furnace slag and rice husk ash: Strength and permeability properties. *Journal of Cleaner Production, 205*, 49–57. https://doi.org/10.1016/J.JCLEPRO.2018.08.313

Mohammed, A. A., Nahazanan, H., Nasir, N. A. M., Huseien, G. F., Saad, A. H., Mohammed, A. A., Nahazanan, H., Azline, N., Nasir, M., Huseien, G. F., & Saad, A. H. (2020). Calcium-based binders in concrete or soil stabilization: Challenges, problems, and calcined clay as partial replacement to produce low-carbon cement. *Materials., 2023*, 16. https://doi.org/10.3390/MA16052020

Mundra, S., Bernal, S. A., Criado, M., Hlaváček, P., Ebell, G., Reinemann, S., Gluth, G. J. G., & Provis, J. (2017). Steel corrosion in reinforced alkali-activated materials. *RILEM Technical Letters, 2*, 33–39. https://doi.org/10.21809/rilemtechlett.2017.39

Nazari, A., Sanjayan, JG. Handbook of low carbon concrete, Kidlington, UK, 2017.

Nazari Sam, M., Schneider, J., & Lutze, H. V. (2023). Modelling porous cementitious media with/without integrated latent heat storage: Application scenario. *Energies (Basel), 16*, 6687. https://doi.org/10.3390/EN16186687/S1

Nematollahi, B., Sanjayan, J., Qiu, J., & Yang, E. H. (2017). Micromechanics-based investigation of a sustainable ambient temperature cured one-part strain hardening geopolymer composite. *Construction and Building Materials, 131*, 552–563. https://doi.org/10.1016/j.conbuildmat.2016.11.117

Noushini, A., & Castel, A. (2018). Performance-based criteria to assess the suitability of geopolymer concrete in marine environments using modified ASTM C1202 and ASTM C1556 methods. *Materials and Structures*. https://doi.org/10.1617/s11527-018-1267-z

Noushini, A., Nguyen, Q. D., & Castel, A. (2021). Assessing alkali-activated concrete performance in chloride environments using NT Build 492. *Materials and Structures*. https://doi.org/10.1617/s11527-021-01652-7

NTB 492, Concrete, Mortar and cement-based repair materials: chloride migration coefficient from non-steady-state migration experiments, (1999) 8.

Ojo, J. O., spsampsps Mohr, B. J. A review of the analysis of cement hydration kinetics via 1H nuclear magnetic resonance. In: Nanotechnology in Construction 3, Springer Berlin Heidelberg, 2009: pp. 107–112. https://doi.org/10.1007/978-3-642-00980-8_13.

Oligschläger, D., Kupferschläger, K., Poschadel, T., Watzlaw, J., & Blümich, B. (2014). Miniature mobile NMR sensors for material testing and moisture-monitoring. *Diffusion Fundamentals*. https://doi.org/10.62721/diffusion-fundamentals.22.834

Ouellet-Plamondon, C., & Habert, G. (2015). *Life cycle assessment (LCA) of alkali-activated cements and concretes*. Woodhead Publishing Limited. https://doi.org/10.1533/9781782422884.5.663

Perez-Cortes, P., & Escalante-Garcia, J. I. (2020). Alkali activated metakaolin with high limestone contents – Statistical modeling of strength and environmental and cost analyses. *Cement and Concrete Composites, 106*, 103450. https://doi.org/10.1016/j.cemconcomp.2019.103450

Robayo-Salazar, R., Mejía-Arcila, J., Mejía de Gutiérrez, R., & Martínez, E. (2018). Life cycle assessment (LCA) of an alkali-activated binary concrete based on natural volcanic pozzolan: A comparative analysis to OPC concrete. *Construction and Building Materials, 176*, 103–111. https://doi.org/10.1016/j.conbuildmat.2018.05.017

Runci, A., & Serdar, M. (2022). Effect of curing time on the chloride diffusion of alkali-activated slag. *Case Studies in Construction Materials, 16*, e00927. https://doi.org/10.1016/J.CSCM.2022.E00927

Ryukhtin, V., Slížková, Z., Strunz, P., Bauerová, P., Frankeová, D., & Ilavsky, J. (2023). Microstructural changes in building materials after various consolidation treatments studied by small-angle neutron scattering, mercury intrusion porosimetry and scanning electron microscopy. *Journal of Applied Crystallography, 56*, 976–987. https://doi.org/10.1107/S1600576723005320

Salami, B. A., Ibrahim, M., Al-Osta, M. A., Nasir, M., Ali, M. R., Bahraq, A. A., & Wasiu, A. (2023). Engineered and green natural pozzolan-nano silica-based alkali-activated concrete: Shrinkage characteristics and life cycle assessment. *Environmental Science and Pollution Research, 30*, 17840–17853. https://doi.org/10.1007/s11356-022-23424-8

Salami, B. A., Johari, M. A. M., Ahmad, Z. A., & Maslehuddin, M. (2017b). POFA-engineered alkali-activated cementitious composite performance in acid environment. *Journal of Advanced Concrete Technology, 15*, 684–699. https://doi.org/10.3151/JACT.15.684

Salami, B. A., Maslehuddin, M., & Mohammed, I. (2014). Mechanical properties and durability characteristics of SCC incorporating crushed limestone powder. *J Sustain Cem Based Mater, 4*, 176–193. https://doi.org/10.1080/21650373.2014.990068

Salami, B. A., Megat Johari, M. A., Ahmad, Z. A., & Maslehuddin, M. (2016). Impact of added water and superplasticizer on early compressive strength of selected mixtures of palm oil fuel ash-based engineered geopolymer composites. *Construction Building Materials., 109*, 198–206. https://doi.org/10.1016/j.conbuildmat.2016.01.033

Salami, B. A., Megat Johari, M. A., Ahmad, Z. A., & Maslehuddin, M. (2017a). Durability performance of Palm Oil Fuel Ash-based Engineered Alkaline-activated Cementitious Composite (POFA-EACC) mortar in sulfate environment. *Construction Building Materials, 131*, 229–244. https://doi.org/10.1016/j.conbuildmat.2016.11.048

Salami, B. A., Megat Johari, M. A., Ahmad, Z. A., Maslehuddin, M., & Adewumi, A. A. (2018). Impact of Al(OH)3 addition to POFA on the compressive strength of POFA alkali-activated mortar. *Construction Building Materials., 190*, 65–82. https://doi.org/10.1016/j.conbuildmat.2018.09.076

Schwab, K. The global competitiveness report 2018, in: World Economic Forum, 2018.
Stern, M., & Geary, A. L. (1957). Electrochemical polarization I. *A Theoretical Analysis of the Shape of Polarization Curves, J Electrochem Soc, 104*, 56–63.
Tabish, M., Zaheer, M. M., & Baqi, A. (2023). Effect of nano-silica on mechanical, microstructural and durability properties of cement-based materials: A review. *Journal of Building Engineering, 65*, 105676. https://doi.org/10.1016/j.jobe.2022.105676
Tennakoon, C., Shayan, A., Sanjayan, J. G., & Xu, A. (2017). Chloride ingress and steel corrosion in geopolymer concrete based on long term tests. *Materials & Design, 116*, 287–299. https://doi.org/10.1016/j.matdes.2016.12.030
Toma, I. O., Stoian, G., Rusu, M. M., Ardelean, I., Cimpoeşu, N., & Alexa-Stratulat, S. M. (2023). Analysis of pore structure in cement pastes with micronized natural zeolite. *Materials., 16*, 4500. https://doi.org/10.3390/MA16134500
Tran, N. P., Gunasekara, C., Law, D. W., Houshyar, S., Setunge, S., & Cwirzen, A. (2021). A critical review on drying shrinkage mitigation strategies in cement-based materials. *Journal of Building Engineering, 38*, 102210. https://doi.org/10.1016/j.jobe.2021.102210
Valori, A. (2009). *Characterisation of cementitious materials by 1H NMR*. University of Surrey.
Weise, K., Endell, L. M., Ukrainczyk, N., & Koenders, E. (2024). Pozzolanic metakaolin reactivity: Time-dependent influence of calcium hydroxide, alkali hydroxides, and sulfates. *Construction and Building Materials, 431*, 136534. https://doi.org/10.1016/J.CONBUILDMAT.2024.136534
Xu, C., Gong, Y., & Yan, G. (2023a). Research on cement demand forecast and low carbon development strategy in Shandong province. *Atmosphere (Basel), 14*, 267. https://doi.org/10.3390/atmos14020267
Xu, Z., Ma, Y., Wang, J., & Shen, X. (2023b). Preparation and hydration properties of steel slag-based composite cementitious materials with high strength. *Materials, 16*, 2764. https://doi.org/10.3390/ma16072764
Xue, C., Sirivivatnanon, V., Nezhad, A., & Zhao, Q. (2023). Comparisons of alkali-activated binder concrete (ABC) with OPC concrete-a review. *Cement and Concrete Composites, 135*, 104851. https://doi.org/10.1016/j.cemconcomp.2022.104851
Yang, H., Monasterio, M., Zheng, D., Cui, H., Tang, W., Bao, X., & Chen, X. (2021). Effects of nano silica on the properties of cement-based materials: A comprehensive review. *Construction and Building Materials, 282*, 122715. https://doi.org/10.1016/j.conbuildmat.2021.122715
Zhang, J., & Li, Z. (2009). Application of GEM equation in microstructure characterization of cement-based materials. *Journal of Materials in Civil Engineering, 21*, 648–656. https://doi.org/10.1061/(asce)0899-1561(2009)21:11(648)
Zhang, J., Ma, Y., Zheng, J., Hu, J., Fu, J., Zhang, Z., & Wang, H. (2020). Chloride diffusion in alkali-activated fly ash/slag concretes: Role of slag content, water/binder ratio, alkali content and sand-aggregate ratio. *Construction and Building Materials, 261*, 119940. https://doi.org/10.1016/j.conbuildmat.2020.119940
Zhou, B., Ma, Q., Guo, R., & Li, P. (2024). Chloride permeability of alkali-activated slag concretes after exposure to high temperatures. *Materials, 17*, 1028. https://doi.org/10.3390/ma17051028

Publisher's Note

Mohammed Ibrahim Research Engineer in Applied Research Center for Metrology, Standards and Testing, Research Institute, King Fahd University of Petroleum & Minerals, Dhahran 31261, Saudi Arabia.

Ashraf A. Bahraq Post-Doctoral Fellow in Interdisciplinary Research Center for Construction and Building Materials, King Fahd University of Petroleum & Minerals, Dhahran 31261, Saudi Arabia.

Babatunde Abiodun Salami Senior Lecturer in Cardiff School of Management, Cardiff Metropolitan University (Landaff Campus), Cardiff, CF5 2YB, United Kingdom.

Luai Mohammed Alhems Professor in Applied Research Center for Metrology, Standards and Testing, Research Institute, King Fahd University of Petroleum & Minerals, Dhahran 31261, Saudi Arabia.

Syed Rizwanullah Hussaini Research Engineer in Centre for Integrative Petroleum Research, College of Petroleum Engineering & Geosciences, King Fahd University of Petroleum & Minerals, Dhahran 31261, Saudi Arabia.

Muhammad Nasir Lecturer in Department of Civil and Construction Engineering, College of Engineering, Imam Abdulrahman Bin Faisal University, Dammam, 31451, Saudi Arabia.

Adeshina Adewale Adewumi Lecturer in Department of Civil Engineering, University of Hafr Al Batin, 31991 Hafr Al-Batin, Saudi Arabia.